ACS OMEGA

Open Access

http://pubs.acs.org/journal/acsodf

Article

Relative Investigation on Microwave-Assisted Zr-Modified $PbTiO_3$ and $BaTiO_3$ Ferroelectric Ceramics for Energy Storage Application

Chinmay Chandan Parhi, Avanish Babu Thirumalasetty, Ajit Raymond James, and Madhuri Wuppulluri*

Cite This: *ACS Omega* 2023, 8, 37752−37768

Read Online

ACCESS | Metrics & More | Article Recommendations | Supporting Information

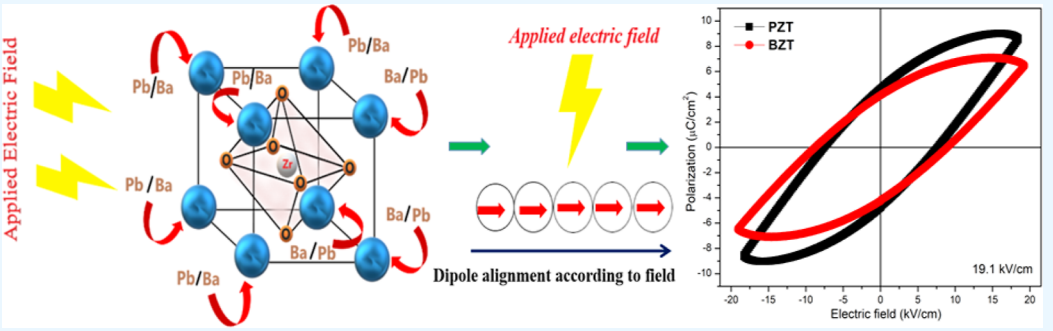

ABSTRACT: The escalating demand for energy-related devices has prompted an intensive study on materials for energy harvesting and storage. Recently, due to the toxicity of lead-based materials, researchers have drawn their attention to lead-free ferroelectrics. However, it is indisputable that commercially lead zirconium titanate (PZT) has gained an irreplaceable position as an actuator. In the present work, we specifically compare microwave-sintered $PbZr_{0.52}Ti_{0.48}O_3$ and $BaZr_{0.20}Ti_{0.80}O_3$ ceramics based on their energy-storage capacity. The structural, optical, electrical, ferroelectric, and energy storage properties of microwave-sintered Zr-modified lead titanate ($PbZr_{0.52}Ti_{0.48}O_3$, PZT) and Zr-modified barium titanate ($BaZr_{0.20}Ti_{0.80}O_3$, BZT) ceramics are investigated and addressed. The temperature-dependent dielectric property analysis suggests high transition temperature and dielectric properties for PZT ceramic, whereas the near-room temperature transition is observed in the case of BZT. Furthermore, the band-gap energy value of BZT and PZT from UV−vis spectroscopy indicates the possible use of these ceramics in optoelectronic devices. The ferroelectric properties of PZT and BZT are discussed, and the maximum energy storage capacities are found to be 30.5 and 21 mJ/cm^3 for PZT and BZT, respectively. It is found that microwave-sintered PZT's characteristics make it an attractive option for use in filters, phase shifters, sensors, actuators, and energy-related devices. On the other hand, BZT finds its suitability in biomedical devices and underwater applications.

INTRODUCTION

The presence of ferroelectricity in any system is mainly due to the structure of the system, in other words, the symmetry of the unit cell. Some dielectric materials do not possess a center of symmetry. As a result, these materials exhibit piezoelectric properties. Piezoelectricity is a physical phenomenon that arises when stress causes charge separation in the material. Also, when a material is exposed to an electric field, it undergoes mechanical strain.[1] Materials with ferroelectricity have several useful properties such as permittivity, high piezoelectric coefficient, field varying polarization high electro-optic effect, and pyroelectric coefficients. Based on the applications, ferroelectric materials can be made in various forms such as thin-film, bulk ceramics, and polymer composites. Technologically significant ferroelectrics are oxide compounds with the structure of perovskite. This distortion of perovskite cubic structure leads to ferroelectricity in materials. Ferroelectric distortion leads to a small displacement of cations with respect to anions, which results in a net dipole moment for each unit volume.[2] It is well known that, perovskite structures when left undistorted above Curie temperature results in non-ferroelectric materials. On the other hand, below T_c (Curie temperature), the distorted perovskite cubic structure gives rise to the ferroelectric capabilities of the materials. Based on this, ferroelectric materials are classified according to the structural modification at the transition temperature.[3] Recently, the scientific community has been focusing on the order−disorder "eight-site model".[4] According to this model, the cubic phase comprises a random distortion along cubic diagonals or [111] direction. The tetragonal phase has displacement with

Received: October 20, 2022
Accepted: August 30, 2023
Published: October 5, 2023

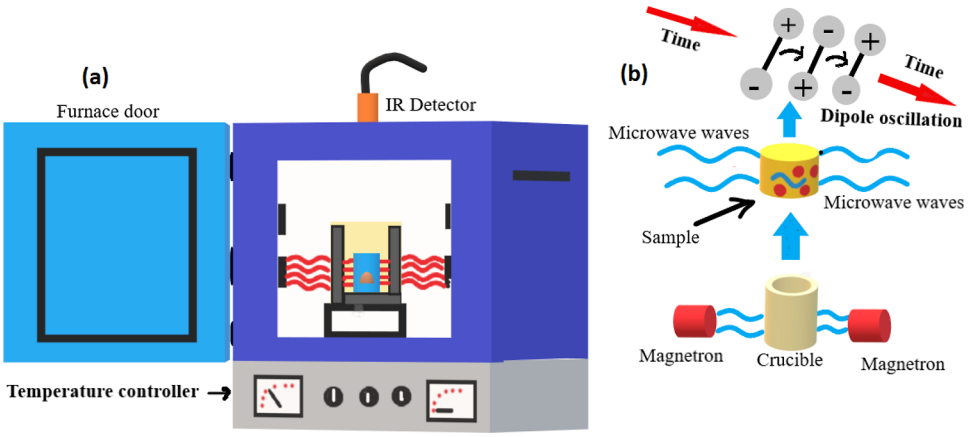

Figure 1. (a) Schematic illustration of microwave furnace and (b) working principle of microwave sintering.

polarization in the [100] direction, the orthorhombic has two occupied sites and polarization along [110], and the rhombohedral phase along [111]. So far, the piezoelectric and ferroelectric characteristics of dielectric ceramics are being extensively researched due to their energy storage density. Given their long lifespan, rapid charge-discharging ability, and high power density, dielectric capacitors are crucial in industries that deal with energy conversion. From day-to-day life to the military industry, dielectric ceramics with high storage density are of great importance. An appropriate dielectric capacitor that can replace the current storage devices is the state of art.

In spite of the toxic environmental effects, lead-based ferroelectric perovskite materials attracted many researchers due to their high piezoelectric properties. $PbZr_xTi_{1-x}O_3$ (lead zirconium titanate, PZT) is a perovskite structured material, having a general chemical formula ABO_3. It is the combination of the antiferroelectric phase of $PbZrO_3$ with a rhombohedral structure and the ferroelectric phase of $PbTiO_3$ with a tetragonal structure.[5] The formation of PZT can be enhanced depending upon the sintering temperature.[6] PZT finds its application in sensors, transducers, transformers, bandpass filters, and non-volatile memory devices.[7] PZT with high Zr concentrations has *R*3*m* and *R*3*c* space groups of which *R*3*m* is a high-temperature phase, whereas *R*3*c* is a low-temperature phase. PZT exhibits rhombohedral *R*3*m* and tetragonal *P*4*mm* space group. Various researchers have synthesized PZT in different routes such as Cho et al. synthesized PZT through the sol−gel technique[8] and Geetika et al. and Nayak et al. prepared PZT using a normal solid-state reaction technique.[9,10] Furthermore, Wang et al. synthesized thick films of PZT through the hydrothermal route.[11]

Recent studies indicate that the scientific community is looking for alternate lead-free ferroelectric materials with enhanced dielectric constant, and low dielectric loss. This led to perovskite-structured $BaTiO_3$-based materials with good dielectric and ferroelectric attributes,[12] high electromechanical couplings, and a high d_{33} value.[13] The addition of Zr in BTO leads to more chemical stability which results in a high dielectric constant and high ferroelectric properties.[14] Furthermore, on enhancing the concentration of Zr, T_c decreases. From the literature, it is known that lead-free ferroelectrics like BZT can be used as energy harvesters[15] and ferroelectric relaxors.[16]

Ferroelectricity in both Zr-modified $BaTiO_3$ (BZT) and $PbTiO_3$ (PZT) perovskite-structured materials arises essentially due to hybridization between the 3d states of titanium and 2p states of oxygen. Barium and oxygen interaction in BTO-based ferroelectric is ionic and favors the rhombohedral phase. On the other hand, the hybridization of lead and oxygen in PTO-based ferroelectrics results in the stabilization of the tetragonal structure. In BTO ceramics, Ba does not have a 5p hybridization and valence band, whereas in the case of $PbTiO_3$, there is a strong interaction between lead and oxygen. The small size of Pb^{+2} and large strain in PTO results in the stabilization of the cubic phase. In lead titanate, the dipolar electron density around lead results in increased ferroelectric distortion, while in barium-titanate, barium does not polarize along with ferroelectric distortion.[2]

In the current investigation, microwave sintering is used to sinter the ceramics by using microwave radiation, which lowers the power consumption and sintering time. The interaction between material and microwave radiation results in dipole oscillation which leads to the self-heating of the materials. Microwave sintering has more advantages compared to the conventional way of sintering. The microwave sintering technique not only reduces the processing time and sintering temperature but also improves the electrical properties, density, and microstructure of the material. Therefore, in this work, microwave sintering is utilized to synthesize PZT and BZT. So far, there is no literature available for microwave sintered BZT and PZT in terms of energy storage capacity. Figure 1 illustrates the schematic diagram of the microwave furnace and the pictorial representation of the working principle self-heating process.[16] Previously, there are several reports of microwave-sintered modified $PbTiO_3$[16−18] and $BaTiO_3$.[19,20]

The present article gives a detailed comparison of zirconium modified PTO and BTO for the benefit of design engineers to select appropriate materials according to applications. This kind of comparative study is the first of its kind. Furthermore, this work checks the feasibility and efficiency of lead-free and lead based titanates for energy storage applications. Furthermore, very little literature is available on microwave-sintered titanates and their energy storage properties.

EXPERIMENTAL SECTION

Synthesis of Lead Zirconium Titanate. Lead zirconium titanate ($PbZr_{0.52}Ti_{0.48}O_3$) is prepared through the conven-

https://doi.org/10.1021/acsomega.2c06764
ACS Omega 2023, 8, 37752−37768

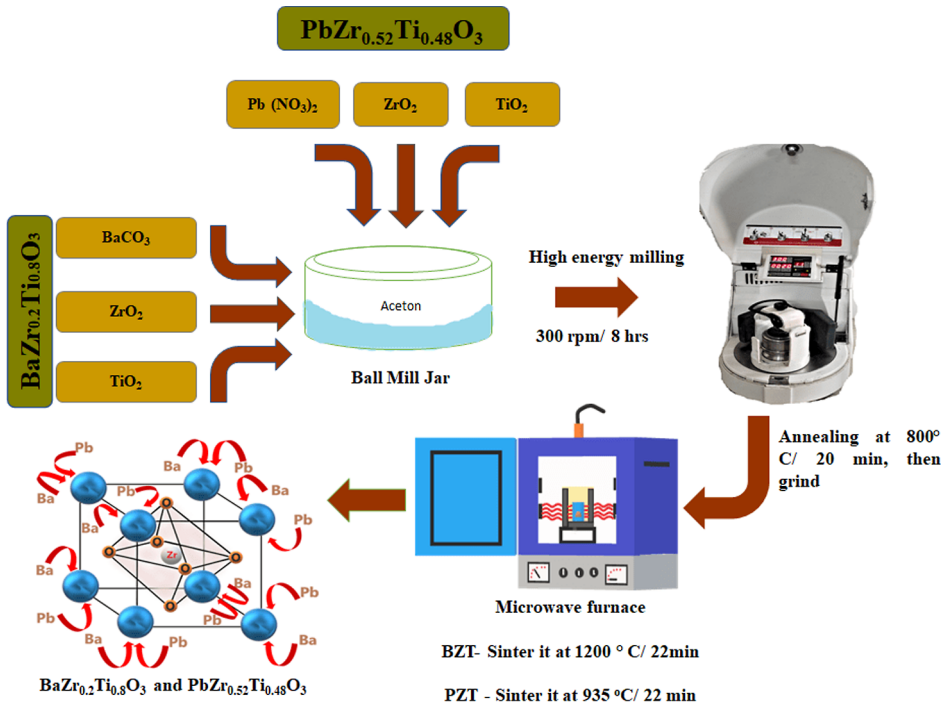

Figure 2. Schematic representation for the synthesis of microwave-sintered PZT and BZT.

tional ceramic method that involves double sintering. The starting materials are $Pb(NO_3)_2$ (lead nitrate), ZrO_2 (zirconium oxide), and TiO_2 (titanium oxide) (AR grade purity, Sigma-Aldrich). These are measured in a definite stoichiometric ratio and powders are grinded in a high energy ball mill using a planetary ball milling system (PULUERISETTE p-6, Fritsch GmbH, Germany). Nitrates are more reactive than oxides and promote densification at relatively low sintering temperatures. The milling is done at 300 rpm for 8 h. The powders so obtained are pressed into pallets with the help of a uniaxial hydraulic press and the prepared pallets are presintered at 500 °C for 20 min using a microwave furnace. The calcined pellet is grinded. To obtain fine particles, the grinded powder is milled for another 8 h in a wet milling medium. Furthermore, the slurry is dried in a hot air oven. The powder is pressed into pellets of a diameter of 10 mm and thickness of 1.2 mm using a hydraulic press at 0.5 ton pressure. These pellets undergo final sintering in the Pb atmosphere and the microwave furnace. The final sintering temperature of 935 °C is maintained for 22 min.

Synthesis of Barium Zirconium Titanate. A regular solid-state technique is used to synthesize barium zirconium titanate ($BaZr_{0.2}Ti_{0.8}O_3$). Barium carbonate, [Sigma-Aldrich (99.9%)], zirconium oxide, [Sigma-Aldrich (99%)], and titanium oxide, [Alfa Aesar (99.5%)] are weighed in the required stoichiometric ratio using an electronic weighing instrument and the measured materials are wet milled using tungsten carbide balls at 300 rpm for 8 h. The slurry so obtained is dried in a hot air oven at 85 °C for 45 min. The obtained dry powder is pressed into pellets through a stainless steel dye set using a hydraulic press. These pallets are calcined at 800 °C for 20 min using a microwave furnace. The green pellets are again ball milled at 300 rpm for 8 h. PVA is added to the dry powder as a binding agent and pressed into pellets of diameter 10 mm and thickness of 1.2 mm using a uniaxial hydraulic press at 0.5 tons. These pellets are finally sintered at 1200 °C for 22 min using a programmable microwave furnace (VBCC, Pvt. Ltd, India). A schematic representation of the above experimental method is illustrated in Figure 2.

With the use of a powder X-ray diffractometer (X'pert, Panalytical, Netherland), the structural features are identified. To ensure the phase transition temperature, thermal analysis of the ceramics is performed at a heating rate of 5 °C/min under an argon atmosphere using TA SDC 650. Scanning electron microscopy (SEM, Thermo Fisher Scientific FEI Quanta 250 FEG, Carl Zeiss, EDX—Oxford-INCx-act) is used to examine the morphology and microstructure of the synthesized PZT and BZT. Furthermore, a UV−vis spectrometer (V. JASCO V-750 PC) is used to estimate the absorption intensity and band gap energy of both samples. To determine the existence of particular groups in $BaZr_{0.2}Ti_{0.8}O_3$ and $PbZr_{0.52}Ti_{0.48}O_3$, FTIR spectroscopy (Fourier transform infrared region) (IR Affinity-1, Shimadzu) is utilized. The sintered pellets are covered on both sides with silver electrodes. The dielectric attributes concerning the temperature of BZT and PZT are studied using an LCR bridge instrument (N4L PSM 1735 and Agilent E4980). To study the electrical characteristics, a high-performance Alpha A frequency analyzer from Novocontrol Technologies (Germany) is used. TF Analyzer 2000, manufactured by aixACT system GmbH (Germany) is used at room temperature to measure the ferroelectric evaluation of $BaZr_{0.2}Ti_{0.8}O_3$ and $PbZr_{0.52}Ti_{0.48}O_3$ utilizing a triangle waveform at 0.1 Hz frequency.

RESULTS AND DISCUSSION

Structural Analysis. The X-ray diffraction (XRD) patterns of microwave-sintered PZT and BZT samples are illustrated in Figure 3 The XRD profile of $BaZr_{0.2}Ti_{0.8}O_3$ and $PbZr_{0.52}Ti_{0.48}O_3$ indicates that both the samples have a pure perovskite phase without any secondary phases or impurity. PZT sintered at 935 °C has a tetragonal crystal structure with a *P4mm* space group. Gonçalves et al.[17] also reported a similar

https://doi.org/10.1021/acsomega.2c06764
ACS Omega 2023, 8, 37752−37768

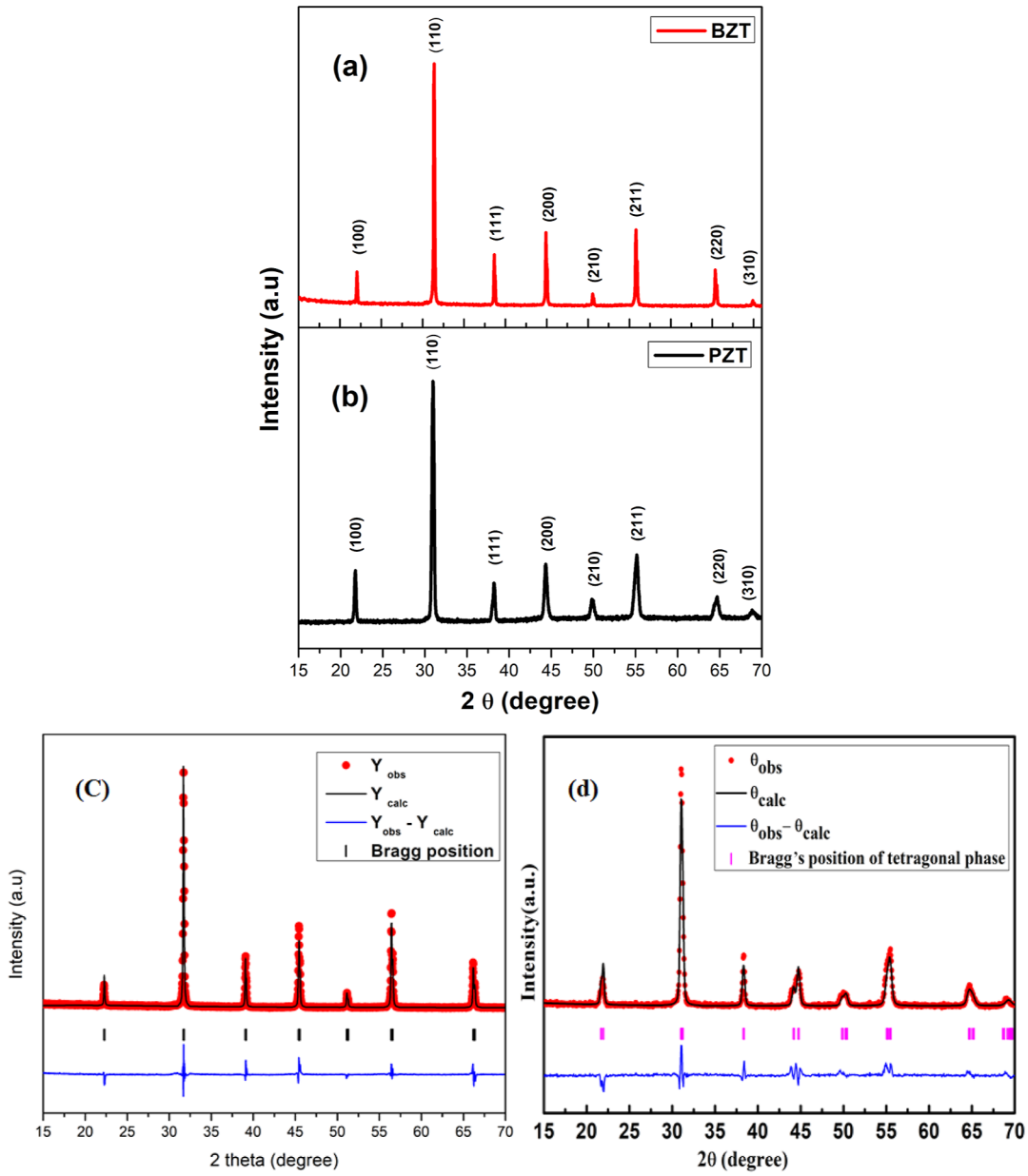

Figure 3. XRD profile of (a) $BaZr_{0.2}Ti_{0.8}O_3$ (1200 °C) and (b) $PbZr_{0.52}Ti_{0.48}O_3$ (935 °C), (c) Rietveld refined XRD pattern of BZT, and (d) Rietveld refined XRD pattern of PZT.

Table 1. Structural Physical Parameters of Microwave-Sintered PZT and BZT

sample	molecular wt. (g)	sintering temp. (°C)	sintering time (min)	avg. grain size (nm)	space group	avg. crystallite size (Å) (%)	lattice parameters (Å)	density (g/cm^3)	relative density (%)
PZT	325.60	935	22	417	*P4mm*	148.9 ± 0.1	$a = b = 4.06 \pm 0.5\%$; $c = 4.109 \pm 0.9\%$	7.7	99.7
BZT	241.86	1200	22	762	*P4mm*	340.86 ± 0.1	$a = b = 3.988 \pm 0.5\%$; $c = 3.994 \pm 0.9\%$	5.48	89.7

structure. It is noticed that 935 °C is the perfect sintering temperature for PZT using microwaves to obtain the perfect phase, which is attributed to the high diffusion of Zr^{4+} ions. BZT ceramics sintered at 1200 °C have a tetragonal phase with a *P4mm* space group. The obtained structural peaks are in good agreement with Cai et al.[21] and Binhayeeniyi et al.[22] reports. The XRD patterns are matched with JCPDS file no. 32-0784 and 75-0461 for $PbZr_{0.52}Ti_{0.48}O_3$ and $BaZr_{0.2}Ti_{0.8}O_3$, respectively. To verify and complete the analysis of XRD, Rietveld refinement of the XRD data is performed to confirm the phase composition of PZT and BZT by fitting the XRD pattern with Pseudo-voigt structural model using FULL-PROOF software. It can be observed that the best fit in refinement for the microwave-sintered BZT ceramic is the tetragonal phase since the lowest goodness of fit is obtained. For microwave-sintered PZT, the best fit in refinement is the tetragonal phase. The summary of the lattice parameters, volumes, and goodness of fit for PZT and BZT obtained by

https://doi.org/10.1021/acsomega.2c06764
ACS Omega 2023, 8, 37752−37768

Table 2. Rietveld Refinment Parameters of PZT and BZT

	PZT	BZT
space group	*P4mm*	*P4mm*
a (Å)	4.06	3.988
b	4.06	3.988
c	4.109	3.994
α (deg)	90	90
β	90	90
γ	90	90
cell volume (Å^3)	67.73	63.54
goodness of fit	3.67	2.89

Table 3. Crystallite Size and Lattice Strain Obtained through W−H Method

	crystallite size (Å) (%)	lattice strain (ε) (10^{-2}) (%)
PZT	118.9 ± 0.1	30.115 ± 0.1
BZT	393.12 ± 0.1	0.113 ± 0.1

Rietveld refinement are listed in Table 2. The reliability parameters are listed in Table S1 of the Supporting Information.

The average crystallite size (D) is calculated using the Scherer equation [eq 1]. Lattice parameters are calculated with the help of Miller indices (h, k, l) and tabulated in Table 1. It is observed that the characteristic peaks in PZT shifted toward a lower angle (2θ) value as compared to the peaks in the case of BZT due to the substitution of Pb^{2+} with Ba^{2+} at the A site of the ABO_3 perovskite structure. Such an observation is due to the difference in the ionic radius of Pb^{2+} and Ba^{2+}; the ionic radius of Pb^{2+} (129 pm) is less than that of Ba^{2+} (142 pm).[23] Therefore, the substitution of Pb^{2+} at the A site replaces Ba^{2+} which can lead to shrinkage in the lattice. The lattice is not able to compensate for the shrinkage which results in the shifting of peaks, which is in agreement with Figure 3. Table 1 also gives the measured densities and relative densities of the samples. The densities of the samples are measured using Archimedes's principle in xylene. While the relative density is the ratio of experimental density to theoretical density estimated from the lattice parameter.

$$\text{Crystallitesize } (D) = \frac{k\lambda}{\beta \cos\theta} \quad (1)$$

The crystallite size of PZT and BZT is estimated through the Williamson−Hall method as well. The W−H plot depends on peak size broadening and strain. The W−H method is an integral breadth technique that determines crystallite size and strain-related line broadening by evaluating the peak width as a function of 2θ.[24] In addition to the crystallite size, lattice strain (ε) which is experienced by the ceramics during the sintering process is estimated. It is observed that the PZT has a higher microstrain as compared to that of BZT. The higher strain in lead based ferroelectrics can be explained on the basis of the smaller ionic radius of Pb^{2+} and lead-oxygen hybridization. Table 3 depicts the crystallite size and lattice strain obtained through the W−H method.

Thermal Analysis. The thermal behavior and temperature-dependent phase transition of PZT and BZT ceramics are represented in Figure 4. It is well established that the crystalline phase formation is an exothermic reaction and the heat flow as a function of temperature for PZT and BZT shows an exothermic reaction peak at the transition temperature. From the figure, it is evident that the BZT has a phase transition temperature near the room temperature, 34 °C, whereas PZT has a phase transition temperature of 330 °C. These phase transition temperatures are in good agreement with the dielectric studies (as shown in Table 4).

Microstructure Analysis. Images produced with the aid of a scanning electron microscope show the well-grown grains of BZT and PZT. In Figure 5, the microstructure of both ceramics are displayed. It is known that ceramics' grain size has a significant impact on the dielectric constant, polarization, resistivity, and Curie temperature. Higher mobility of BZT ions has resulted due to larger grains. Larger grains of BZT is attributed to influence the electrical resistivity of the ceramics.[25] BZT seems to be more porous than PZT as is evident from the SEM images. Such an observation can also be found in XRD results.

The surface morphology of the two samples shows that the materials are more densely packed and that the grains are tightly spaced and regularly arranged. The polycrystalline nature of the samples is reflected by the consistent grain size with apparent grain boundary, resulting in better electrical

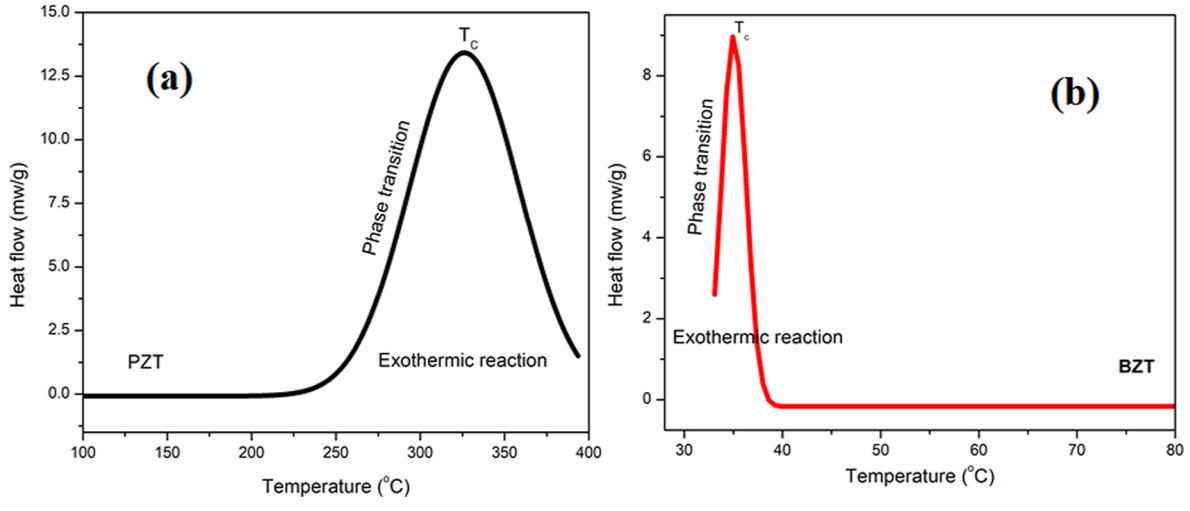

Figure 4. Temperature-dependent heat flow and phase transition of (a) $PbZr_{0.52}Ti_{0.48}O_3$ and (b) $BaZr_{0.2}Ti_{0.8}O_3$.

https://doi.org/10.1021/acsomega.2c06764
ACS Omega 2023, 8, 37752−37768

Table 4. Dielectric and Electrical Parameters of Microwave-Sintered PZT and BZT

sample	T_c (°C)	T_c (°C)			room temperature				
		ε_r at 1 MHz	tan δ at 1 MHz	tan δ at 1 kHz	σ_{ac} (S/cm) at 1 MHz	σ_{ac} (S/cm) at 1 kHz	|Z| (ohm) at 1 MHz	ε_r at 1 MHz	tan δ at 1 kHz
PZT	341	3429	0.069	0.027	46.81×10^{-5}	5.053×10^{-7}	66.6×10^{6}	802.5	0.021
BZT	31	12,200	0.75	0.026	26.11×10^{-5}	3.02×10^{-7}	37.07×10^{4}	445	0.211

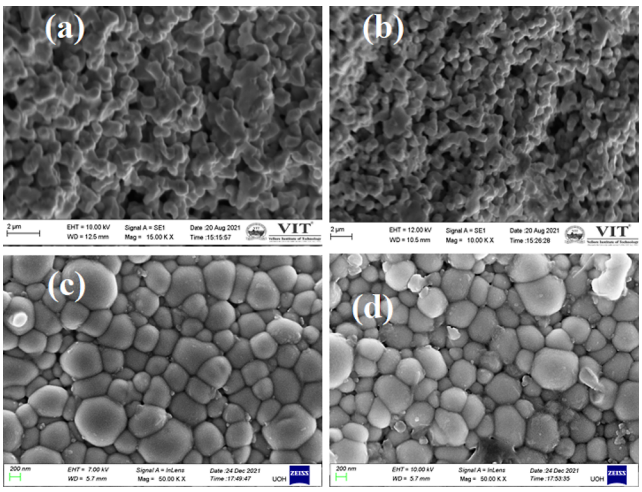

Figure 5. Scanning electron microscopy images of (a) $BaZr_{0.2}Ti_{0.8}O_3$ (BZT) at 15k× magnification and (b) BZT at 10k× magnification, (c) $PbZr_{0.52}Ti_{0.48}O_3$ (PZT) at 50k× magnification, and (d) PZT at 50k× magnification (PZT).

characteristics. Using ImageJ software, the grain size distribution curve is depicted in Figure 6 along with the estimates of the grain size distribution for BZT and PZT. Table 1 shows the typical average grain size of BZT and PZT. Furthermore, the energy-dispersed spectra for $PbZr_{0.52}Ti_{0.48}O_3$ and $BaZr_{0.2}Ti_{0.8}O_3$ assured that all required components are present in the materials without any contaminants. The EDS spectrum demonstrates that the solid state reaction is complete for the formation of the perovskites (shown in Figure 7). The EDS technique is only a qualitative analytical method, which confirms the existence and distribution of the desired elements (as illustrated in Figure 7a,b in microwave-sintered PZT and BZT).

UV−Vis Spectroscopy. The behavior of both ferroelectrics is studied in the UV−vis region. The absorbance coefficient and scattering coefficient are estimated from diffused reflectance spectra. Both the ferroelectric materials show maximum absorbance between 330 and 335 nm which corresponds to the near UV region. The band gap of PZT and BZT is determined by extrapolating the straight-line portion onto the photon energy ($h\nu$) axis as shown in Figure 8. The directly allowed energy band gap (E_g) of these ferroelectrics has been estimated from the correlation between the incident photon energy ($h\nu$) and the coefficient of absorption (α) as given by eq 2. The band gap energy is estimated through the Kubelka−Monk function $f(R)$ using the DRS values.[26]

$$(\alpha h\nu) = B(h\nu - E_g)^n \quad (2)$$

where B is a constant quantity, the exponent $n = 1/2$ for the direct band gap, and $n = 2$ for the indirect band gap. The presence of lead in $PbZr_{0.52}Ti_{0.48}O_3$ (PZT) at the A site and higher doping concentration of Zr results in a minutely lower band gap energy value in comparison to $BaZr_{0.2}Ti_{0.8}O_3$ (BZT). The band gap value obtained for PZT is 3.08 eV and for BZT is 3.14 eV. PZT and BZT energy band gaps are determined from linear optical absorption spectra and found to be well within the UV region, allowing them to be employed as filters in optoelectronic devices in the blue region.

FTIR Spectroscopy. Energy absorption and the presence of constituent bond stretching are indicated by the FTIR profile. Figure 9 shows the Fourier transformation IR spectrum of BZT and PZT. The BO_6 octahedron of the ABO_3 perovskite structures, such as $BaTiO_3$, $PbTiO_3$, $ZrTiO_3$, etc., comprises a variety of vibrations, at high-frequency ν_1 (Ti−O or Zr−O), low-frequency ν_2 (Ti−O_3 or Zr−O_3), and bending ν_3 (Ti−O_3 or Zr−O_3) (O−Ti−O, O−Zr−O). All the corresponding peaks related to ν_1, ν_2, and ν_3 are observed in both ceramics. The BO_6 octahedra found inside the perovskite structure are

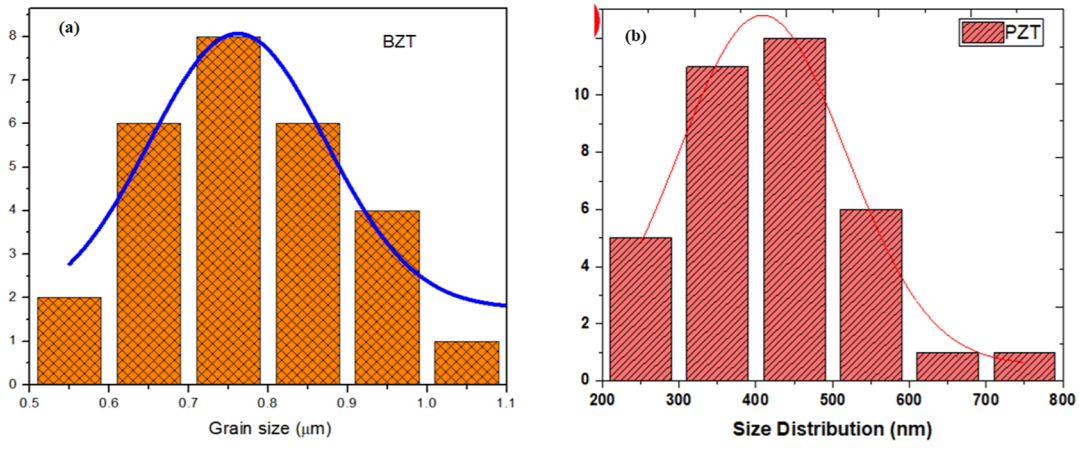

Figure 6. Grain size distribution plots of (a) $BaZr_{0.2}Ti_{0.8}O_3$ and (b) $PbZr_{0.52}Ti_{0.48}O_3$.

https://doi.org/10.1021/acsomega.2c06764
ACS Omega 2023, 8, 37752−37768

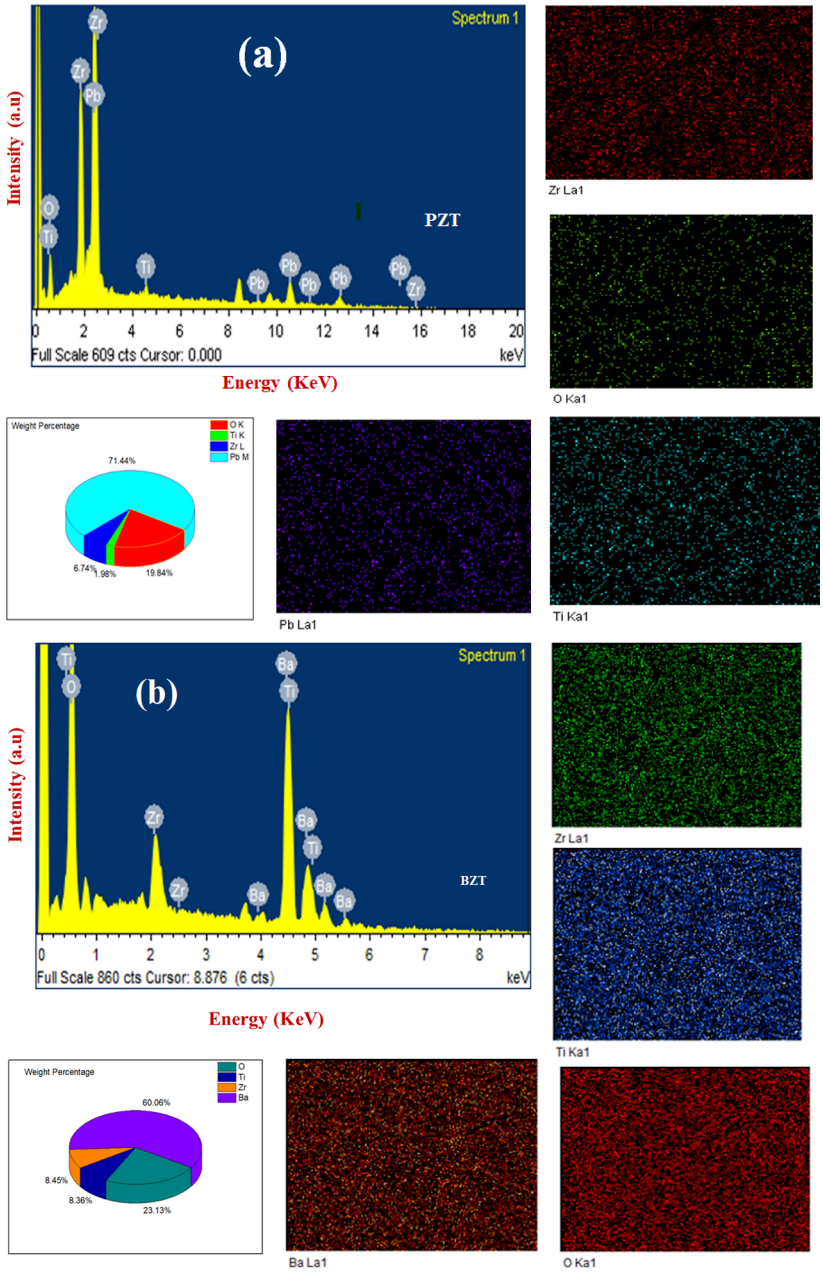

Figure 7. EDS spectrum and elemental mapping of (a) $PbZr_{0.52}Ti_{0.48}O_3$ and (b) $BaZr_{0.2}Ti_{0.8}O_3$.

evident from the broad peaks in both samples. This represents metal−oxygen linkage. Narrow peaks can be seen in the FTIR profile when Ba is substituted for Pb at site A of the ABO_3 perovskite structure. It is known that the shortest Ti−O (186 pm) and Ba−O (279 pm) lengths in BZT are longer than the shortest Ti−O (178 pm) and Pb−O (253 pm) distances in PZT. This discrepancy could explain the peak narrowing.[27] FT-IR spectra of BZT sintered at 1200 °C exhibit peaks from 400 to 600 cm^{-1}, which corresponds to Zr−O and Ti−O stretching vibrations. The Ti−O absorption band (bending vibration) and the $BaCO_3$ fingerprint are correlated with the stretching of 439.77 cm^{-1}. The Zr−O_6 octahedral connection and the Ti−O octahedra's vibration cause a vibrational stretching at 503.42 cm^{-1}. As per the XRD data, the shifting of peaks in the FT-IR spectra of both PZT and BZT ceramics exhibits modest changes in lattice parameters. The existence of vibrational peaks around 790 cm^{-1} in both BZT and PZT supports the creation of a perovskite structure which is also supported by XRD results.

Dielectric Property Analysis. *Temperature and Frequency-Dependent Dielectric Properties.* The dielectric behavior of the ceramics is investigated in terms of dielectric constant and dielectric loss, which is temperature- and frequency-dependent. The temperature dependence of relative permittivity, ϵ_r (dielectric constant), and dielectric loss factor (tan δ) of BZT and PZT, in the frequency range 1 kHz to 1 MHz, as shown in Figure 10 (1 kHz, 10 kHz, 100 kHz, 1 MHz). In the temperature range of 30 to 400 °C for $PbZr_{0.52}Ti_{0.48}O_3$ and 27 to 100 °C for $BaZr_{0.2}Ti_{0.8}O_3$, the frequency dependency of ϵ_r and tan δ is investigated. Table 4 represents the dielectric parameters of PZT and BZT. The relative permittivity or dielectric constant of PZT progressively rises with the temperature at a given frequency, as seen from the ϵ_r−T curve (Figure 10). The ϵ_r value has a very modest rise

https://doi.org/10.1021/acsomega.2c06764
ACS Omega 2023, 8, 37752−37768

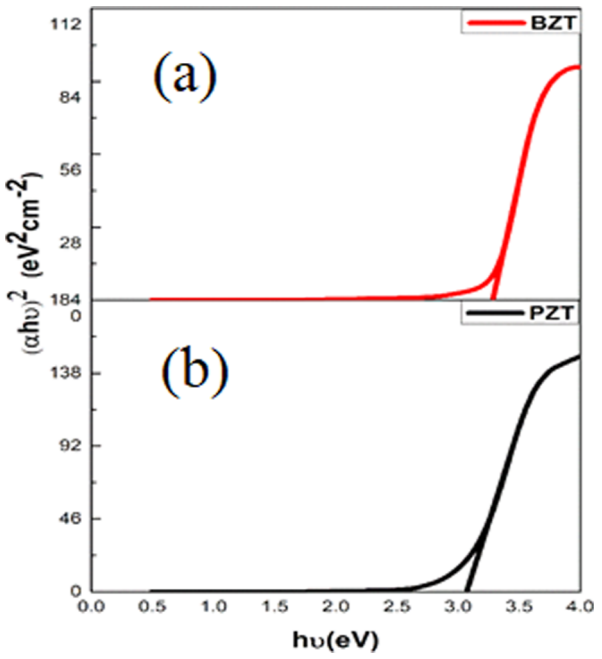

Figure 8. Tauc's plot for (a) $BaZr_{0.2}Ti_{0.8}O_3$ and (b) $PbZr_{0.52}Ti_{0.48}O_3$.

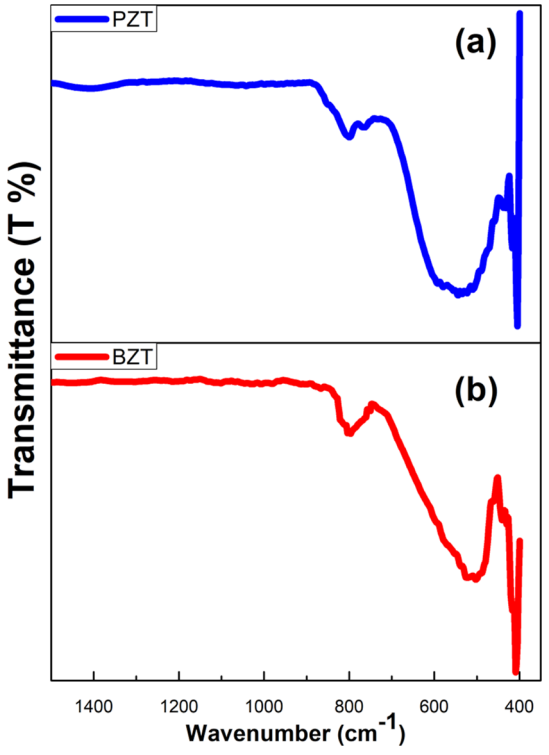

Figure 9. FT-IR spectra for (a) PZT and (b) BZT.

from 40 to 250 °C and is nearly constant. This is due to weak and constant feedback of the charge carriers at this range of temperatures.[28] Beyond 250 °C, a steep rise of ϵ_r is noticed. At 1 MHz, PZT has a maximum ϵ_r value of 3796, which is higher than previously reported values.[29] The Curie transition temperature is found to be 341 °C, beyond which the dielectric constant decreases. The Curie transition temperature is established owing to the phase transition of ceramics from the ferroelectric phase to the paraelectric phase. In the case of PZT, a diffused transition is noticed. This is due to the complex occupation of the A site and the B site in the ABO_3 structure by Pb^{2+}, Zr^{4+}, and Ti^{4+} ions. The dielectric loss corresponding to microwave sintered PZT at 1 kHz is 0.06.

Similarly, BZT exhibits an almost constant ϵ_r value from 27 to 30 °C attributed to weak reaction from the charge carriers. A maximum ϵ_r value of 12,200 is observed at 31 °C at 1 MHz owing to sharp ferro to para phase transition at this temperature, beyond which the dielectric constant decreases (as shown in Figure 10). Similar results are observed in previous reports.[22,30] The decrease in ϵ_r value after Curie transition temperature in ferroelectric ceramics attributes to the disorientation of the thermally agitated dipoles from the applied electric field.[15,31] The microwave sintered BZT exhibits a similar trend for tan δ versus temperature and a relaxation peak is noticed at T_c. Both BZT and PZT ceramics exhibits dielectric relaxation which is attributed to the thermally activated ferroelectric dipoles.

Figure 11 indicates the frequency dependence relative permittivity and dielectric loss of BZT and PZT in the frequency range of 1 Hz to 1.5 MHz. In the lower frequency range, both permittivity and dielectric loss have a higher value which gradually decreases with the increase in frequency. At lower frequencies, all types of polarization contribute to the dielectric constant of the ceramics. With the gradual increase in frequency, the contribution of dipolar polarization and atomic polarization vanishes, respectively, and at higher frequency regions only electronic polarization contributes to the dielectric constant of the ceramics. Therefore, the dielectric constant decreases with an increase in frequency.[32] A plateau behavior of ϵ_r noticed in the lower and high-frequency range of both BZT and PZT is attributed to the extrinsic offering from grain as well as the grain boundary effect.[33] At low frequencies, the space charge and the diploes oscillate and follow the applied field. Furthermore, according to Maxwell−Wagner theory, conducting grains are separated by insulating grain boundaries. This results in a large local polarization of grains leading to a higher ϵ_r at lower frequencies.[34] As frequency increases, due to inertia, dipoles cannot respond to the applied field and do not contribute to the net polarization. Hence, the dielectric constant decreases exponentially only as electronic polarization contributes to net polarization.

Confined charge carriers of ferroelectric ceramics absorb energy and break the grain boundary resulting in higher conductivity. A similar trend is observed in tan δ as a function of frequency (Figure 11). The presence of d.c. conductivity is indicated by the quick increase in the dielectric loss at a lower frequency. The loss factor is produced at lower frequencies by the ion mobility within the material. Dielectric loss occurs at moderate to high-frequency range as a result of ion jump, ion polarization loss, conduction loss due to ion migration, and, accordingly, ion vibration.[35,36] Dielectric breakdown and conduction mechanisms are strongly related. In the case of PZT and BZT, both lattices are modified by introducing Zr. The unit cell has enlarged as a result of the Zr addition, which increases further net polarization. Additionally, it is noted that the dielectric loss factor ceases to depend on frequency from 10 kHz onward, which is evident from Figure 11.

The ferroelectric distortion involves cation displacement relative to anions, which leads to a net dipole moment per unit volume. As a result of Pb−O hybridization [6s of (Pb) and 2p of (O)], Ti−O [3d (Ti) and 2p (O)], and Zr−O hybridization, a larger ferroelastic strain is required in PZT to sustain the tetragonal phase than that of BZT because as

https://doi.org/10.1021/acsomega.2c06764
ACS Omega 2023, 8, 37752−37768

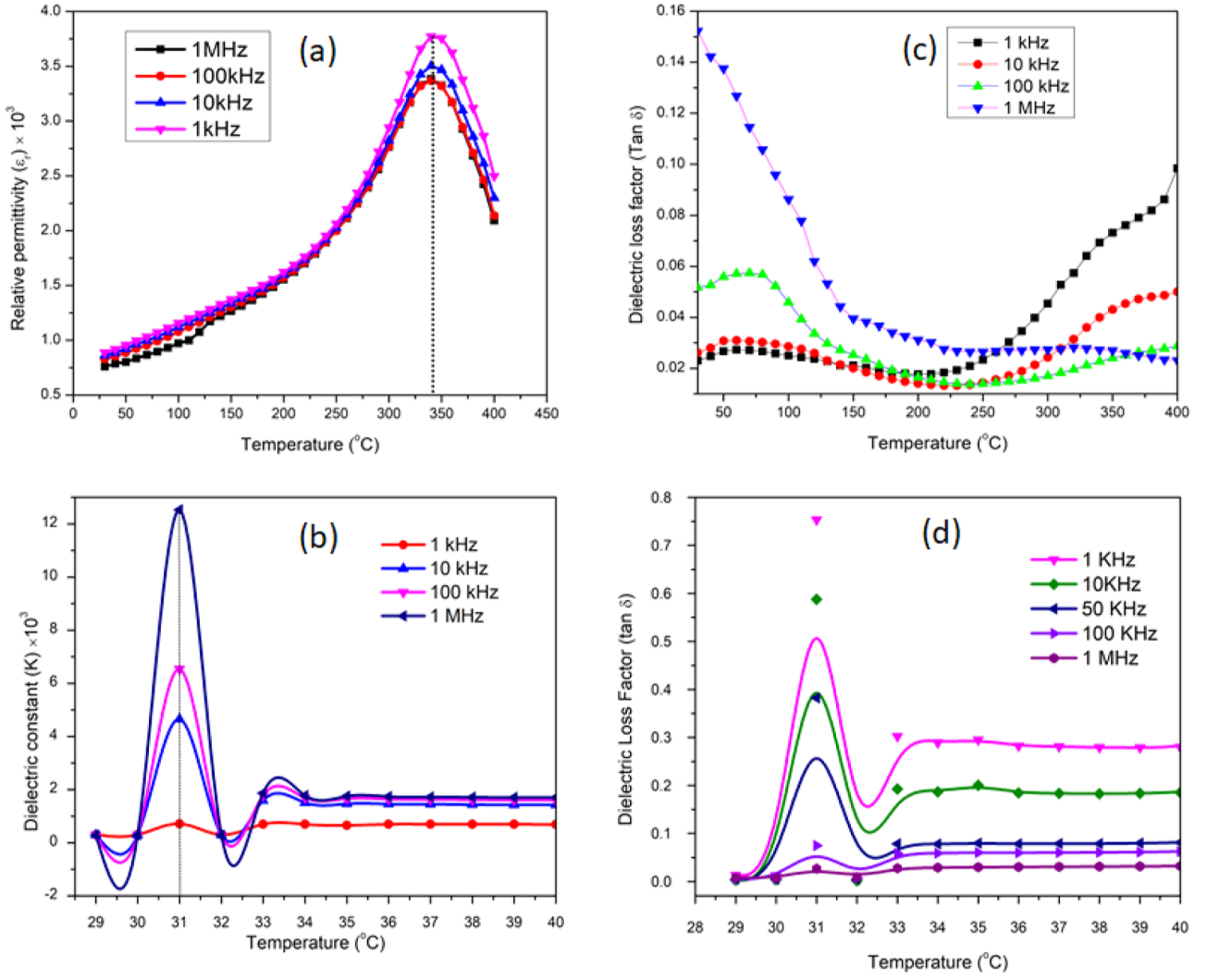

Figure 10. Temperature dependence of relative permittivity of (a) $PbZr_{0.52}Ti_{0.48}O_3$, (b) $BaZr_{0.2}Ti_{0.8}O_3$, and tan δ (dielectric loss) of (c) $PbZr_{0.52}Ti_{0.48}O_3$ and (d) $BaZr_{0.2}Ti_{0.8}O_3$.

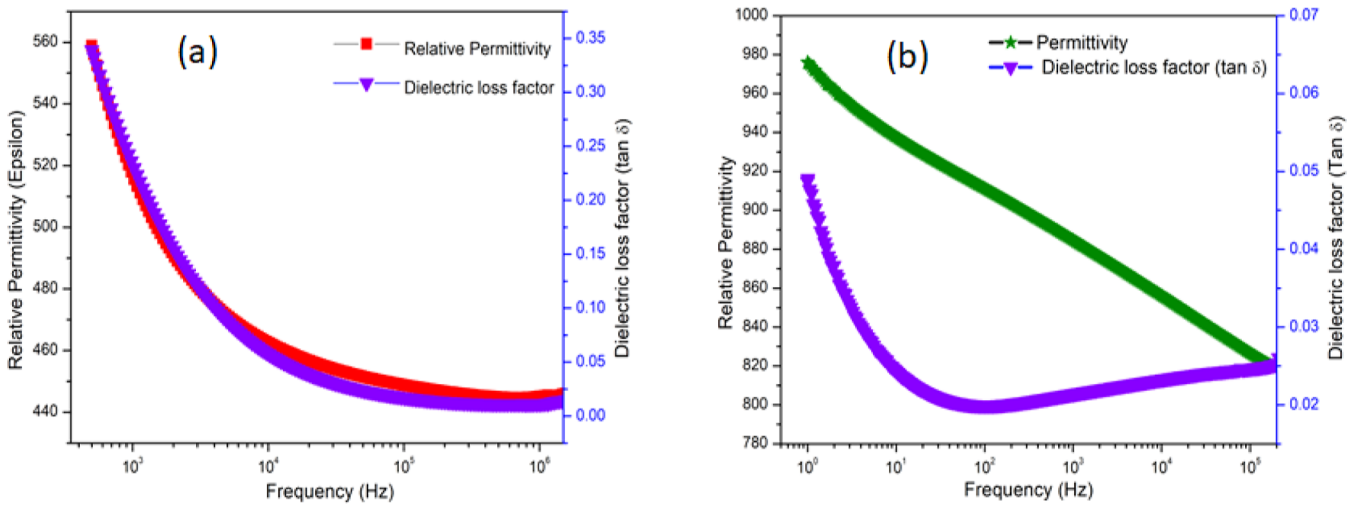

Figure 11. Frequency dependence of permittivity and dielectric loss (tan δ) at room temperature of (a) $BaZr_{0.2}Ti_{0.8}O_3$ and (b) $PbZr_{0.52}Ti_{0.48}O_3$.

compared to Ba^{2+}, Pb^{2+} has a smaller ionic radius.[2] An ordered tetragonal phase in PZT was stabilized at higher temperatures by substantial strain. BZT features a low-temperature transition with an unstable tetragonal phase due to tiny strain and ferroelectric distortion. Higher strain in PZT compared to BZT is evident from the XRD results. This strain modifies the

https://doi.org/10.1021/acsomega.2c06764
ACS Omega 2023, 8, 37752−37768

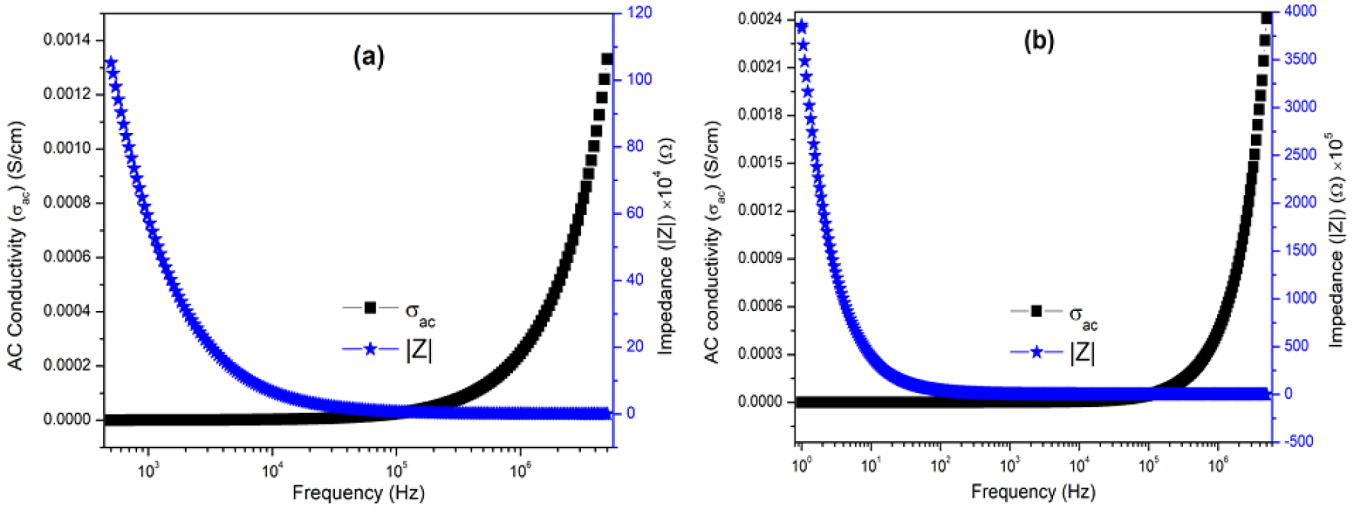

Figure 12. AC conductivity (σ_{ac}) and impedance |Z| as a function of frequency (a) $BaZr_{0.2}Ti_{0.8}O_3$ and (b) $PbZr_{0.52}Ti_{0.48}O_3$.

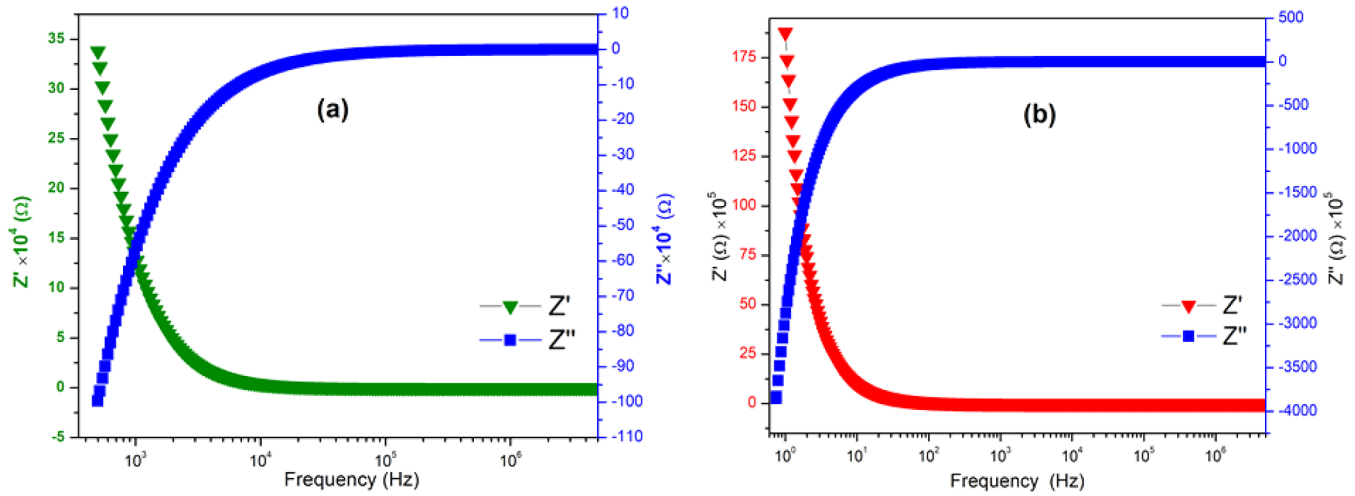

Figure 13. Real part (Z') and imaginary part (Z'') of complex impedance as function of frequency (a) $BaZr_{0.2}Ti_{0.8}O_3$ and (b) $PbZr_{0.52}Ti_{0.48}O_3$.

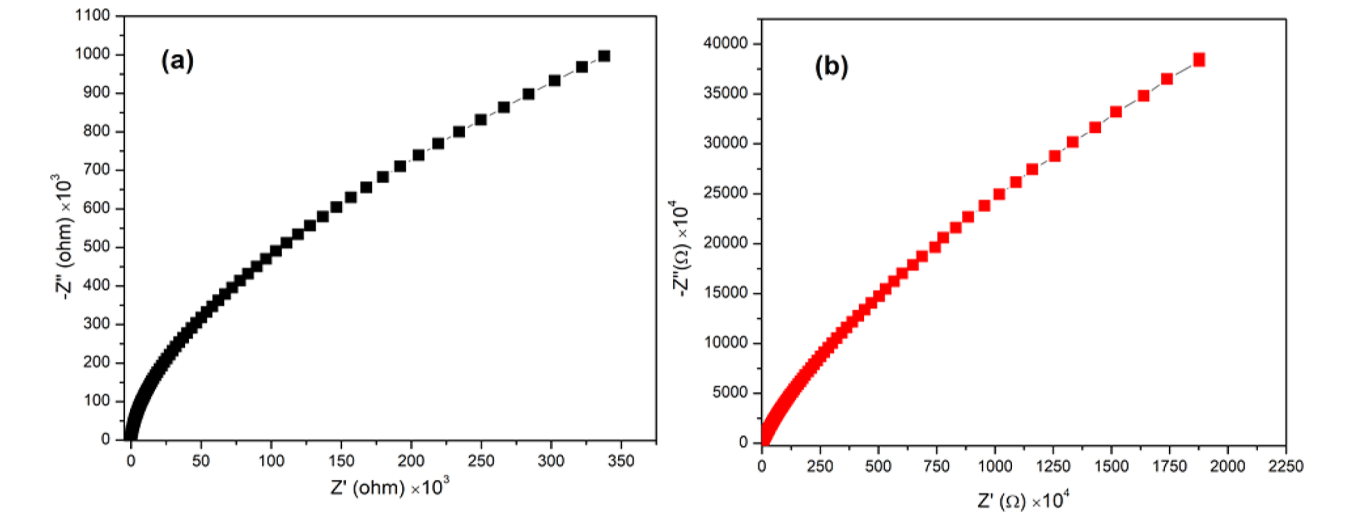

Figure 14. Cole−Cole plots of (a) $BaZr_{0.2}Ti_{0.8}O_3$ and (b) $PbZr_{0.52}Ti_{0.48}O_3$.

equilibrium phase diagram and disturbs the local fluctuation in ferroelectric phases.[37] Zr-substituted $BaTiO_3$ has the dielectric and ferroelectric transition from the cubic phase to tetragonal in low temperature, whereas Zr-modified PTO has cubic to tetragonal phase at a higher temperature range. It is observed that the Curie transition temperature (T_c) of BTO and PTO decreases to a lower value upon doping of Zr at the B site of perovskite structured $PbTiO_3$ and $BaTiO_3$. T_c is known to

https://doi.org/10.1021/acsomega.2c06764
ACS Omega 2023, 8, 37752−37768

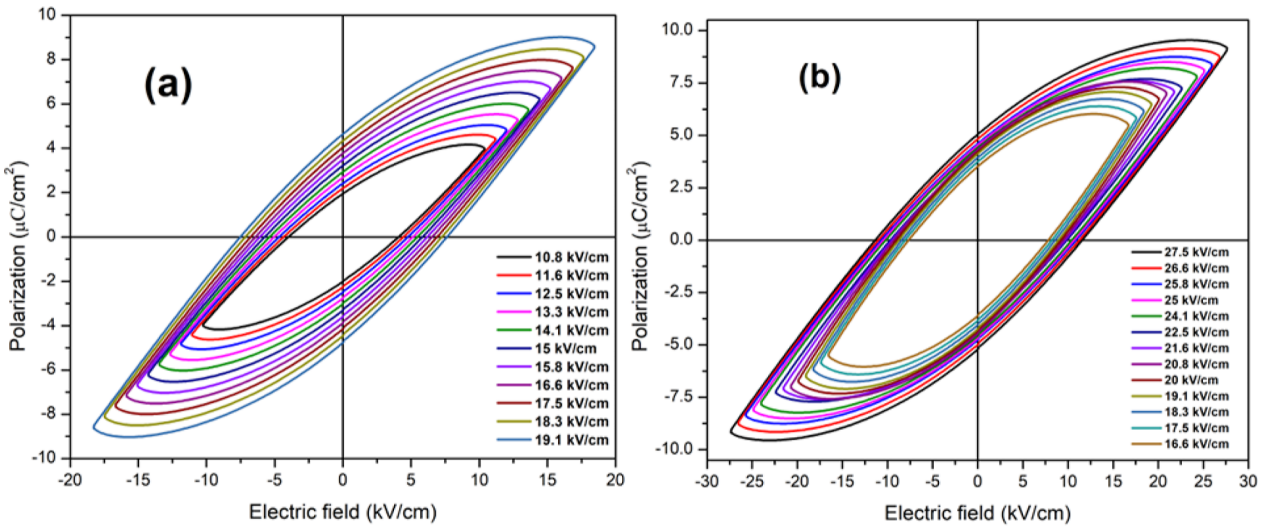

Figure 15. Polarization as a function of electric field plot for (a) $PbZr_{0.52}Ti_{0.48}O_3$ and (b) $BaZr_{0.2}Ti_{0.8}O_3$.

Table 5. Ferroelectric and Energy Storage Properties of Microwave-Sintered PZT and BZT at an Applied Voltage of 2.3 kV (Applied Electric Field = 19.1 kV/cm)

sample	max. polarization ($2P_m$) (μC/cm^2)	remanent polarization ($2P_r$) (μC/cm^2)	coercive field ($2E_c$) (kV/cm)	curve squareness (R_{sq})	W_{rec} (J/cm^3)	W_{loss} (J/cm^3)	η (%) (efficiency)
PZT	18.73	9.26	15.42	0.795	0.035	0.095	24.4
BZT	14.21	8.22	18.03	0.721	0.021	0.087	19.31

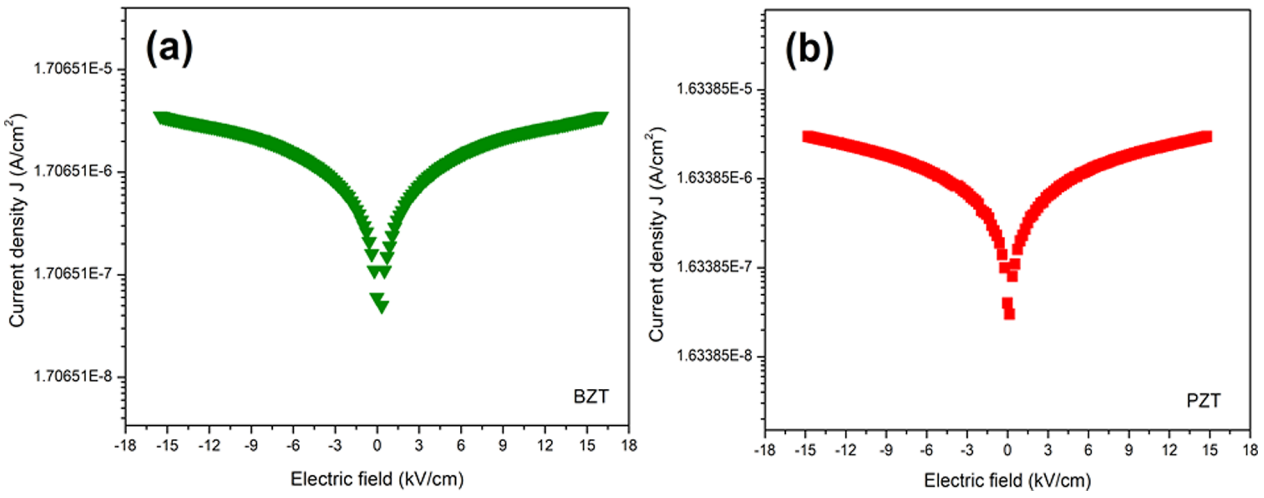

Figure 16. Current density as a function of electric field for (a) $BaZr_{0.2}Ti_{0.8}O_3$ and (b) $PbZr_{0.52}Ti_{0.48}O_3$.

decrease with the addition of Zr due to the wider radius of Zr^{4+} (72 pm). Zr^{4+} substitution for Ti^{4+} (60 pm) may reduce the extent of the B site ion's displacement in oxygen octahedral structures. As a result, the T_c of the perovskite falls and the interaction between B site ions and O^{2-} becomes weak.[35]

Electrical Properties. Figure 12 represents the variation of AC conductivity and absolute impedance as a function of frequency for BZT and PZT. The electrical parameters at room temperature are tabulated in Table 4. The AC conductivity is measured through the following equation.[38] where

$$\sigma_{ac} = \left(\frac{1}{Z} \times \frac{t}{A}\right) \quad (3)$$

$$Z^*(\omega) = Z' - Z'' = R_s - \frac{j}{\omega C_s} \quad (4)$$

Here, C_s and R_s are the series capacitance and resistance, and $\omega = 2\pi f$ is the angular frequency. $1/Z$ represents admittance (Y) at a given frequency, and t and A indicate the thickness and electrode area, respectively. For AC conductivity of ferroelectric materials like PZT and BZT, the fundamental mechanism involves a short-range charge carrier moving back and forth between oxygen vacancy traps, separated by various energy barrier heights.[39] The effect of space charge polarization gradually diminishes with the increase in frequency, and the overall contribution of electric polarization rises. As a result, the AC conductivity rises with the increase in frequency. It is clear from Figure 12 that the AC conductivity decreases when the frequency is lowered. Conductivity becomes frequency-independent after 10 kHz. PZT has a larger AC conductivity value as compared to BZT. The presence of irregular-shaped

https://doi.org/10.1021/acsomega.2c06764
ACS Omega 2023, 8, 37752−37768

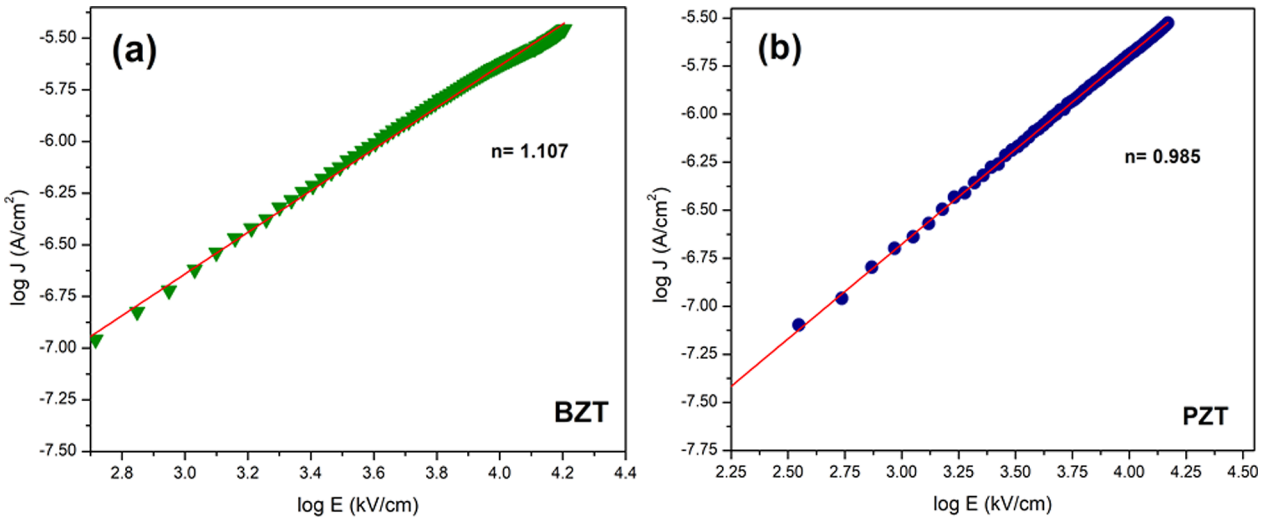

Figure 17. Log J as a function of log E for (a) $BaZr_{0.2}Ti_{0.8}O_3$ and (b) $PbZr_{0.52}Ti_{0.48}O_3$.

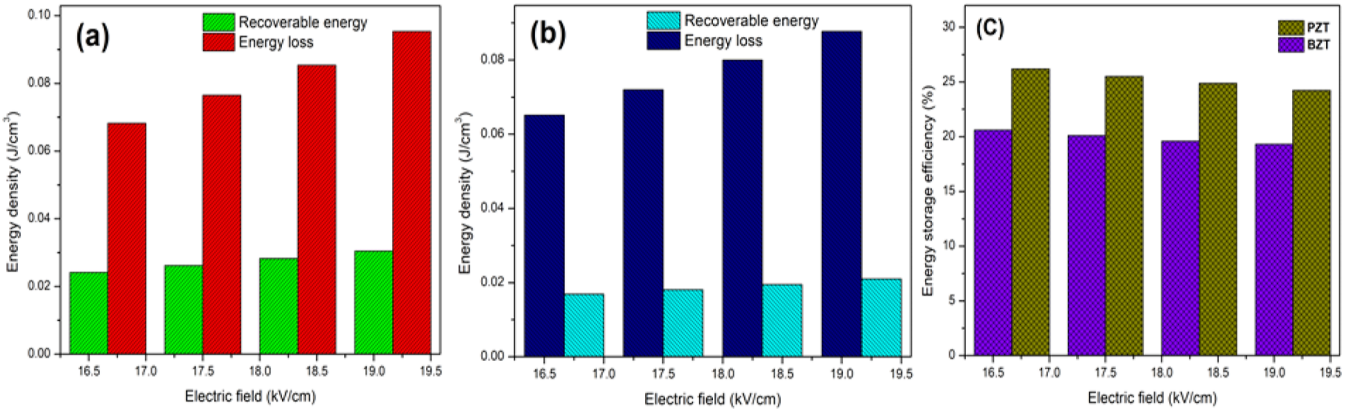

Figure 18. Energy density as a function of applied electric field (a) $PbZr_{0.52}Ti_{0.48}O_3$ and (b) $BaZr_{0.2}Ti_{0.8}O_3$ and (c) energy storage efficiency for PZT and BZT.

Table 6. Efficiency and Energy Density of Microwave-Sintered (a) PZT and (b) BZT

electric field (kV/cm)	charge density (mJ/cm^3)	discharge density (mJ/cm^3)	efficiency (η) %
	(a) PZT		
19.1	30.5	95.3	24.24
18.3	28.3	85.4	24.89
17.5	26.2	76.5	25.51
16.6	24.2	68.2	26.19
15.8	22.3	60.4	26.96
15	20.4	52.9	27.83
	(b) BZT		
27.5	42.7	154.9	21.60
26.6	40.1	143.9	21.79
19.1	21	87.7	19.31
18.3	19.5	80	19.59
17.5	18.1	72	20.08
16.6	16.9	65.1	20.60

grains evident from SEM images (Figure 5) and the difference in ionic radius of Pb^{2+} and Ba^{2+} could be responsible for less AC conductivity in BZT. Improved ion mobility due to prominent grain boundary in PZT enhances the AC conductivity and impedance as compared to $BaZr_{0.2}Ti_{0.8}O_3$. The electrical properties of the ferroelectric ceramics are investigated using the complex impedance spectroscopy (CIS) method at room temperature. CIS helps in analyzing the electrical properties to establish the correlation between the electrical behavior of ceramics and their microstructures. The electrical parameters like AC conductivity and complex impedance (Z' and Z'') of both the electro-ceramics BZT and PZT are examined in the frequency range of 1 Hz to 5 MHz. The complex impedance is measured using eq 4.[39] Figure 13 illustrates the real part (Z') and the imaginary part of impedance (Z'') as a function of frequency for both the ceramics. It is assured from the plots (in Figure 13) that the Z' has a higher value in the low-frequency range. With an increase in frequency, Z' decreases gradually and attains an almost constant value beyond a certain frequency. Z'' shows a similarly gradual decreasing trend as a function of frequency. Due to the impedance's dependence on capacitance and inductance, and also the change in capacitance with respect to frequency, Z' is larger at low frequencies and decreases at higher frequencies. The inductance is frequency-dependent and constant. So, like permittivity (as shown in Figure 11), impedance shows a similar change with frequency. As displayed in Table 4, lead-based PZT ceramics sintered in the microwave have a higher impedance value when compared to the impedance of microwave-sintered lead-free BZT. This is due to the difference in a lattice structure and higher-order distortion in

https://doi.org/10.1021/acsomega.2c06764
ACS Omega 2023, 8, 37752−37768

Table 7. Comparison of Properties of Conventional and Microwave-Sintered Lead-Based PZT and Lead-Free BZT Ferroelectric Compositions

	sintering condition	average grain size	T_m (°C)	ε_r	P_r (μC/cm^2)	energy storage	references
$BaZr_{0.2}Ti_{0.8}O_3$	1350°C/2 h (conventional sintering)	7 μm	39	13,000	2.5		Cheng et al[56]
$BaZr_{0.}2Ti_{0.8}O_3$	2.5 kW/20 min (microwave sintering)	15−40 μm	−10	2200	4.44		Cai et al[21]
$BaZr_{0.3}Ti_{0.7}O_3$	1500°C/3 h (conventional sintering)	6.9 μm		15,000		68% (40 kV/cm)	Liu et al[57]
$BaZr_{0.05}Ti_{0.95}O_3$	1200°C/4 h (conventional sintering)	7 μm		1550	1.15	44% (20 kV/cm)	Badapanda et al[58]
$BaZr_{0.2}Ti_{0.8}O_3$	**1200°C/22 min** (microwave sintering)	**762 nm**	**31**	**12,200**	**4.82**	21.79% **(26.6 kV/cm)**	**present work**
$PbZr_{0.52}Ti_{0.48}O_3$	1100°C/20 min (microwave sintering)	0.5 μm	375	2593			Venugopal Reddy et al[29]
$PbZr_{0.52}Ti_{0.48}O_3$	1000°C/30 min (microwave sintering)	7 μm	400	14,000	13		Venkata Ramana et al[44]
$PbZr_{0.52}Ti_{0.48}O_3$	1200°C/45 min (microwave sintering)		400	20,000	26.69	40 mJ/cm^3 (30 kV/cm)	Samanta et al[26]
$Pb_{0.92}La_{0.08}Zr_{0.52}Ti_{0.48}O_3$	1200°C/45 min (microwave sintering)	0.5 μm	353	10,000	38.45	24% (35 kV/cm)	Samanta et al[59]
$PbZr_{0.52}Ti_{0.48}O_3$	850°C/5 min (Spark plasma sintering)	17 nm	335	1500	3.5	26.1% (25 kV/cm)	Gupta et al[60]
$PbZr_{0.52}Ti_{0.48}O_3$	**935°C/22 min (microwave sintering)**	**417 nm**	**341**	**3429**	**3.21**	27.8% **(15 kV/cm)**	**present work**

the ABO_3 structure as a consequence of Zr doping in $PbTiO_3$. The grain and grain boundary effect plays a major role in complex impedance.

Further complex impedance Cole−Cole plot for BZT and PZT at 300 K is shown in Figure 14 to analyze the electronic transport process. The dielectric relaxation experiment is carried out in the frequency domain, and the values are represented on the complex impedance plane with the aid of the Cole−Cole function. The Cole−Cole establishment can be used to explain the circuit's impedance function (eq 5). Here, τ = RC, and α stands for the relaxation time distribution.[40]

$$Z = \frac{R}{[1 + (i\tau\omega)^{\alpha}]} \tag{5}$$

The value α ranges from 0 to 1 for non-ideal or non-Debye behavior. From Figure 14a,b, it is evident that the complex impedance curves do not exhibit a full semicircle; instead, the semicircle arc is depressed. This indicates the relaxation in BZT and PZT is not of the Debye type. The non-Debye behavior is a result of ionic conduction hopping between fairly random free energy barriers with a wide distribution of relaxation time.[40] This may be because of scattered elements present in the material system.[39] The creation of $PbTiO_3$, $BaTiO_3$, and $ZrTiO_3$ may lead to the development of a linkage among Debye relaxors. The smaller radius of the arc (in Figure 14) in the case of BZT as compared to PZT suggests less contribution from grains than the contribution from grain boundaries. It is a result of the low density of BZT (Table 1) and the existence of porosity that reduces connectivity in grains and confirms the contribution from insulating grain boundaries.[41] This causes a substantial space charge to accumulate at the grain boundaries, as shown by the strong dielectric dispersion in low frequency range as shown in Figure 11.

Ferroelectric Properties. Polarization is monitored when the electric field is changing to determine the ferroelectric property. The ferroelectricity in PZT and BZT is caused by the off-centering of Ti^{4+}/Zr^{4+} ions in TiO_6/ZrO_6 octahedra, which is in good agreement with results from FT-IR analysis. To comprehend the ferroelectric properties of both ceramics, ferroelectric hysteresis in different applied electric fields is explored. Figure 15 shows for PZT and BZT the polarization as a function of the electric field. It is evident from Figure 15 that PZT has larger maximum polarization (P_{max}), remnant polarization (P_r) value, and smaller coercive field (E_c) value compared to P_{max} and E_c of BZT and at the same applied electric field. The internal stress and internal biasing of the electric field, which have an impact on domain reorientation and backflipping of domains, lead the actual polarization in ceramics to be always lower than the expected values. It is well known that the combination of macropolar and micropolar regions considerably increased the diffused phase transition effect, which is why the PZT exhibits a thin $P-E$ hysteresis loop compared to that of BZT.[18] Furthermore, it is observed that due to the uneven grain size and grain boundary in BZT, proven by microstructural investigations, the $P-E$ curve is not saturated properly at 19.1 kV/cm. With an increase of the applied electric field, the polarization curve of BZT as a function of the electric field tends toward saturation. On the other hand, the homogeneously distributed spherical grains with uniform grain sizes and higher density in PZT result in a sharp-edged $P-E$ loop at 2.3 kV applied voltage.[42] Due to low density in BZT, the polarization versus electric field loop is not saturated properly at 2.3 kV. It is well known that the $P-E$ curve for a perfect ferroelectric is a square loop. The squareness of the loop is also related to the ferroelectric ceramic's constituents and homogeneity of grain size. The squareness of the $P-E$ curve and quantity of changes in the hysteresis behavior of ceramics can be calculated using eq 6.[43]

$$R_{sq} = \frac{P_r}{P_s} + \frac{P_{1.1E_c}}{P_r} \tag{6}$$

Here, R_{sq} is the squareness of the hysteresis curve, and $P_{1.1E_C}$ is the polarization at 1.1 times of coercive field. It is confirmed from the increased value of squareness that the ferroelectricity

https://doi.org/10.1021/acsomega.2c06764
ACS Omega 2023, 8, 37752−37768

is increasing from BZT to PZT due to improved domain alignment in the direction of the applied field.

The $P-E$ plot confirmed that the microwave sintered PZT is a soft ferroelectric ceramic with less coercive field, whereas the microwave-sintered BZT has higher E_c as compared to PZT. Such an observation is similar to the results reported by Venkata Ramana et al.[44] Smaller coercive field makes the ferroelectric ceramics suitable for switching applications. The ferroelectric parameters investigated are tabulated in Table 5. Large polarization in microwave sintered Zr modified PTO (PZT) is due to Pb^{2+} occupying the A site. This distorts the structure, and furthermore, the presence of lead vacancy in the system makes domain wall motion easier.[45] This notable low coercive field is beneficial for device applications due to less power loss and low switching voltages.

The leakage current density characteristic measurements have been carried out for microwave sintered lead-based and lead-free ferroelectric ceramics. The current density (J) as a function of electric field (E) curves for BZT and PZT measured at room temperature in an applied field of 0 to ± 16.6 kV/cm are illustrated in Figure 16. Both forward and reverse bias conditions are used to measure the current density characteristics of PZT and BZT. The leakage current density is found to be relatively low and symmetric on applying both negative and positive electric fields ($J < 10^{-5}$ A/cm^2). It is observed from the $J-E$ curves that the leakage current in BZT is higher than that of PZT. It is attributed to higher porosity in BZT (as shown in Table 1). It is previously reported that, in ferroelectric ceramics, pores play a key role in the dielectric breakdown and leakage current.[46,47] The electric field is substantially enhanced when the pores interact with the side of the grains, and if the pores are perpendicular to the field, the electric field between them is increased when they are close to each other. The larger quantity of pores causes a decline in insulation and dielectric breakdown strength which leads to an increase in leakage current density.[48,49] It is well known that in ferroelectric systems, the current density increases with the increase of the electric field.[50] The intrinsic characteristics of ceramics, such as their band gap energies are accountable for the increase in leakage current. Two alternative models, namely, the ohmic conduction model and the space charge limited current model, have been proposed previously to explicate the conduction mechanism in these systems.[51] It is established that there is a direct relation between current density and power law, i.e., $J \propto E^n$. For $n = 1$, the conduction is due to the ohmic conduction mechanism, and for $n = 2$, the conduction mechanism shifts to space charge limited current. To understand PZT and BZT conduction mechanism, the logarithmic relation between current density J and field E is illustrated in Figure 17. From the slopes of PZT $n = 0.9$ and BZT $n = 1.1$ that both microwave sintered ceramics follow ohmic conduction mechanisms. The increased n is attributed to the defects and porosity present in the ceramics.[52]

The $P-E$ curve is used to determine the energy storage density of microwave sintered BZT and PZT ceramics. According to Figure 15, the curve's shape is determined by the change in polarization due to the applied electric field which results in domain switching. Due to the reorientation of the ferroelectric domain, typical ferroelectrics show considerable hysteresis. This causes significant energy loss and reduces the density of recovered energy. Information about energy loss and recoverable energy is obtained from the $P-E$ curve. Wherein the region between P_r to P_{max} branch of the loop and the y-axis represents the recoverable energy (W_{rec}). The closed region under the $P-E$ loop's curve represents energy loss (W_{loss}). The values of W_{rec}, W_{loss}, and efficiency (η) are measured at an applied voltage of 2.3 kV (electric field = 19.1 kV/cm) using eqs 7 and 8. Here, P_{max} and P_r represent the maximum polarization value and remnant polarization respectively. η indicates the efficiency of energy density.[53,54]

$$W_{rec} = \int_{P_m}^{P_s} E \cdot dp \tag{7}$$

$$\eta = \frac{W_{rec}}{W_{loss} + W_{rec}} \tag{8}$$

The difference between maximum polarization (P_{max}) and remnant polarization (P_r), as well as the high breakdown field strength, could explain the larger charge and discharge energy densities. Similar to this, it was observed that the efficiency (η) of ceramics varied depending on the electric fields applied. Although the ceramics charging and discharging energy densities rise linearly as applied electric fields increase, their efficiency gradually decreased due to comparatively bigger P_r and higher leakage current at high electric fields, as shown in Figure 18.

The substantial hysteresis loss in ceramic capacitors causes microwave sintered lead-based and lead-free ceramics to have a limited energy storage density. Bulk ceramics have a low energy storage density as a result of their low squareness of the loop and density breakdown strength. Nonetheless, ferroelectric ceramic capacitors benefit from a high relative permittivity.[55] The recoverable energy density and energy efficiency of PZT is higher than the recoverable energy density and energy efficiency of BZT. The microstructures, grains, and grain boundaries of the ferroelectric play a crucial role in it. Table 6 lists the parameters relating to the density of energy storage. The microstructural, dielectric, ferroelectric, and energy storage properties of microwave sintered BZT and PZT ceramics are compared with other BZT and PZT ceramics and represented in Table 7.

CONCLUSIONS

$PbZr_{0.52}Ti_{0.48}O_3$ and $BaZr_{0.2}Ti_{0.8}O_3$ ceramics with a single phase are synthesized using high energy mechanical milling and microwave sintering. Microwave-assisted sintering reduces processing time (22 min) as well as phase forming temperature. XRD patterns of PZT and BZT concluded the formation of a pure perovskite phase and structural parameters are studied. The thermal property investigation estimated the phase transition temperature for both the ceramics as 34 and 330 °C. Microstructural investigation revealed the well-grown grain structure for both ceramics. UV−vis spectroscopy revealed that the band gap energies of PZT and BZT as 3.08 and 3.14 eV. FT-IR spectroscopy confirms the octahedral metal oxide vibrational frequencies at 503 and 790 cm^{-1} for both ceramics. Temperature-dependent dielectric behavior studies revealed a dielectric constant of 3429 and 12,200 for PZT and BZT at the Curie transition temperature of 341 °C (diffuse) and 31 °C (sharp), respectively, for PZT and BZT. These results are in good agreement with the thermal analysis results. From the complex impedance spectroscopy, it is evident that the microstructures of PZT play a key role in enhancing its electrical properties as compared to BZT. The $P-E$ characterizations revealed the soft ferroelectric nature of

https://doi.org/10.1021/acsomega.2c06764
ACS Omega 2023, 8, 37752−37768

the ceramics. High leakage currents noticed for BZT over PZT are attributed to the high porosity of BZT. Higher energy efficiencies of 24.24 and 19.3% and recoverable energy densities of 35 and 24.3 mJ/cm^3 at an applied voltage of 2.3 kV are noticed for PZT and BZT, respectively. The experimental results indicate that both BZT and PZT are useful for optoelectronic devices and high-frequency applications. In practice, microwave-sintered $PbZr_{0.52}Ti_{0.48}O_3$ can be employed as capacitors, sensors, and energy-related devices. The near-room-temperature phase transition makes microwave-sintered BZT a suitable material for biomedical and underwater applications like SONAR and hydrophone as well as defense applications like acoustic sensors and torpedo detection systems.

■ ASSOCIATED CONTENT

Supporting Information

The Supporting Information is available free of charge at https://pubs.acs.org/doi/10.1021/acsomega.2c06764.

Low-magnification SEM images of for microwave-sintered PZT and BZT and Williamson−Hall plot for PZT and BZT to estimate crystallite size and strain (PDF)

■ AUTHOR INFORMATION

Corresponding Author

Madhuri Wuppulluri − *Center for Functional Materials, Vellore Institute of Technology, Vellore 632014, India;* orcid.org/0000-0002-1650-9931; Email: madhuriw12@hotmail.com

Authors

Chinmay Chandan Parhi − *Department of Physics, School of Advanced Sciences, Vellore Institute of Technology, Vellore 632014, India*

Avanish Babu Thirumalasetty − *Department of Physics, School of Advanced Sciences, Vellore Institute of Technology, Vellore 632014, India*

Ajit Raymond James − *Ceramics and Composites Group, Defence Metallurgical Research Laboratory, Hyderabad 500058, India*

Complete contact information is available at: https://pubs.acs.org/10.1021/acsomega.2c06764

Notes

The authors declare no competing financial interest.

■ ACKNOWLEDGMENTS

The authors gratefully acknowledge two anonymous reviewers and the editor for their constructive comments and valuable suggestions. The authors are thankful to Ceramic Composite Group, Defence Metallurgical Research Laboratory, Hyderabad for supporting and providing characterization facilities. Special thanks to Dr. M.L.V. Mahesh, Sc "D", DMRL, Hyderabad for his valuable inputs and suggestions. Authors are thankful to VIT, Vellore for providing XRD and SEM facilities. Authors are thankful to university of Hyderabad for providing SEM facility.

■ REFERENCES

(1) Jaffe, B.; Cook, W.; Jaffe, H. The piezoelectric effect in ceramics. *Piezoelectr. Ceram.* **1971**, *3*, 7−21.

(2) Cohen, R. E. Origin of ferroelectricity in perovskite oxides. *Nature* **1992**, *358*, 136−138.

(3) Shiozaki, Y.; Nakamura, E.; Mitsui, T. *Ferroelectrics and Related Substances*; Springer, 2001.

(4) Comes, F.; Wenning, U.; Guiner, A. Field predissociation. *J. Phys. Soc. Jpn.* **1970**, *5*, 195−198.

(5) Chen, Y.-T.; Sheu, C.-I.; Lin, S.-C.; Cheng, S.-Y. Effects of microwave heating on dielectric and piezoelectric properties of PZT ceramic tapes. *Ceram. Int.* **2008**, *34*, 621−624.

(6) Necira, Z.; Boutarfaia, A.; Abba, M.; Menasra, H.; Abdessalem, N. Effects of Thermal Conditions in the Phase Formation of Undoped and Doped Pb (Zr 1-x Ti x) O 3 Solid Solutions. *Mater. Sci. Appl.* **2013**, *4*. DOI: 10.4236/msa.2013.45041.

(7) Shkuratov, S. I.; Baird, J.; Antipov, V. G.; Talantsev, E. F.; Chase, J. B.; Hackenberger, W.; Luo, J.; Jo, H. R.; Lynch, C. S. Ultrahigh energy density harvested from domain-engineered relaxor ferroelectric single crystals under high strain rate loading. *Sci. Rep.* **2017**, *7*, 46758−46810.

(8) Yan, Y.; Cho, K.-H.; Priya, S. Identification and effect of secondary phase in MnO2-doped 0.8 Pb (Zr0. 52Ti0. 48) O3−0.2 Pb (Zn1/3Nb2/3) O3 piezoelectric ceramics. *J. Am. Ceram. Soc.* **2011**, *94*, 3953−3959.

(9) Geetika; Umarji, A. The influence of Zr/Ti content on the morphotropic phase boundary in the PZT−PZN system. *Mater. Sci. Eng. B* **2010**, *167*, 171−176.

(10) Nayak, S.; Chaki, T. K.; Khastgir, D. Spherical ferroelectric PbZr0. 52Ti0. 48O3 nanoparticles with high permittivity: Switchable dielectric phase transition with temperature. *Ceram. Int.* **2016**, *42*, 14490−14498.

(11) Wang, D.; Ou-Yang, J.; Guo, W.; Yang, X.; Zhu, B. Novel fabrication of PZT thick films by an oil-bath based hydrothermal method. *Ceram. Int.* **2017**, *43*, 9573−9576.

(12) Li, W.; Xu, Z.; Chu, R.; Fu, P.; Hao, J. Structure and electrical properties of BaTiO3 prepared by sol−gel process. *J. Alloys Compd.* **2009**, *482*, 137−140.

(13) Nguyen, M. D. Ultrahigh energy-storage performance in lead-free BZT thin-films by tuning relaxor behavior. *Mater. Res. Bull.* **2021**, *133*, 111072.

(14) Kuang, S.; Tang, X.; Li, L.; Jiang, Y.; Liu, Q. Influence of Zr dopant on the dielectric properties and Curie temperatures of Ba (ZrxTi1-x) O3 ($0 \le x \le 0.12$) ceramics. *Scr. Mater.* **2009**, *61*, 68−71.

(15) Binhayeeniyi, N.; Sukwisute, P.; Nawae, S.; Muensit, N. Energy conversion capacity of barium zirconate titanate. *Materials* **2020**, *13*, 315.

(16) Avanish Babu, T.; Madhuri, W. Microwave synthesis technique for LTCC and colossal dielectric constant in PZT. *Chem. Phys. Lett.* **2022**, *799*, 139641.

(17) Gonçalves, M. D.; Souza, F. L.; Longo, E.; Leite, E. R.; Camargo, E. R. Dielectric characterization of microwave sintered lead zirconate titanate ceramics. *Ceram. Int.* **2016**, *42*, 14423−14430.

(18) Kumar, A.; Emani, S. R.; James Raju, K.; Ryu, J.; James, A. Investigation of the Effects of Reduced Sintering Temperature on Dielectric, Ferroelectric and Energy Storage Properties of Microwave-Sintered PLZT 8/60/40 Ceramics. *Energies* **2020**, *13*, 6457.

(19) Reddy, S. R.; Prasad, V.; Kumar, P.; Prabahar, K.; Shanker, V.; Roy, S. Microwave sintered lead free ferroelectric BZT-50BCT ceramics with higher Curie temperature and improved dielectric properties. *J. Mater. Sci.: Mater. Electron.* **2018**, *29*, 12451−12456.

(20) Sun, Z.; Pu, Y.; Dong, Z.; Hu, Y.; Liu, X.; Wang, P. Effect of Zr4+ content on the TC range and dielectric and ferroelectric properties of BaZrxTi1- xO3 ceramics prepared by microwave sintering. *Ceram. Int.* **2014**, *40*, 3589−3594.

(21) Cai, W.; Fu, C.; Chen, G.; Deng, X.; Liu, K.; Gao, R. Microstructure, dielectric and ferroelectric properties of barium zirconate titanate ceramics prepared by microwave sintering. *J. Mater. Sci.: Mater. Electron.* **2014**, *25*, 4841−4850.

(22) Binhayeeniyi, N.; Sukvisut, P.; Thanachayanont, C.; Muensit, S. Physical and electromechanical properties of barium zirconium

titanate synthesized at low-sintering temperature. *Mater. Lett.* **2010**, *64*, 305−308.
(23) Shannon, R. D. Revised effective ionic radii and systematic studies of interatomic distances in halides and chalcogenides. *Acta Crystallogr., Sect. A: Cryst. Phys., Diffr., Theor. Gen. Crystallogr.* **1976**, *32*, 751−767.
(24) Basak, M.; Rahman, M. L.; Ahmed, M. F.; Biswas, B.; Sharmin, N. The use of X-ray diffraction peak profile analysis to determine the structural parameters of cobalt ferrite nanoparticles using Debye-Scherrer, Williamson-Hall, Halder-Wagner and Size-strain plot: Different precipitating agent approach. *J. Alloys Compd.* **2022**, *895*, 162694.
(25) Zeng, H.; Wu, Y.; Zhang, J.; Kuang, C.; Yue, M.; Zhou, S. Grain size-dependent electrical resistivity of bulk nanocrystalline Gd metals. *Prog. Nat. Sci.: Mater. Int.* **2013**, *23*, 18−22.
(26) Samanta, S.; Sankaranarayanan, V.; Sethupathi, K. Band gap, piezoelectricity and temperature dependence of differential permittivity and energy storage density of PZT with different Zr/Ti ratios. *Vacuum* **2018**, *156*, 456−462.
(27) Shannon, R. D.; Prewitt, C. T. Effective ionic radii in oxides and fluorides. *Acta Crystallogr., Sect. B: Struct. Crystallogr. Cryst. Chem.* **1969**, *25*, 925−946.
(28) Basha, D. B.; Kumar, N. S.; Kumar, G. R.; et al. Structural, electrical, and magnetic properties of nano Sr1-XLaXFe12O19 (X= 0.2-0.8). *Sci. Rep.* **2022**, *12*, 12723.
(29) Raju, K.; Venugopal Reddy, P. Synthesis and characterization of microwave processed PZT material. *Curr. Appl. Phys.* **2010**, *10*, 31−35.
(30) Kumar, R.; Asokan, K.; Patnaik, S.; Birajdar, B. Evolution of relaxor properties in lanthanum (La) doped barium zirconate titanate. *Ferroelectrics* **2017**, *517*, 8−13.
(31) Parhi, C. C.; W, M. Microwave sintered lead-free ferroelectrics with colossal dielectric constant at optical frequency. *Ferroelectrics* **2022**, *589*, 177−189.
(32) Mahajan, S.; Thakur, O.; Prakash, C.; Sreenivas, K. Effect of Zr on dielectric, ferroelectric and impedance properties of BaTiO3 ceramic. *Bull. Mater. Sci.* **2011**, *34*, 1483−1489.
(33) Coşkun, M.; Polat, Ö.; Coşkun, F. M.; Durmuş, Z.; Çağlar, M.; Türüt, A. The electrical modulus and other dielectric properties by the impedance spectroscopy of LaCrO 3 and LaCr 0.90 Ir 0.10 O 3 perovskites. *RSC Adv.* **2018**, *8*, 4634−4648.
(34) Penchal Reddy, M.; Madhuri, W.; Balakrishnaiah, G.; Ramamanohar Reddy, N.; Siva Kumar, K.; Murthy, V.; Ramakrishna Reddy, R. Microwave sintering of iron deficient Ni−Cu−Zn ferrites for multilayer chip inductors. *Curr. Appl. Phys.* **2011**, *11*, 191−198.
(35) Sarangi, S.; Badapanda, T.; Behera, B.; Anwar, S. Frequency and temperature dependence dielectric behavior of barium zirconate titanate nanocrystalline powder obtained by mechanochemical synthesis. *J. Mater. Sci.: Mater. Electron.* **2013**, *24*, 4033−4042.
(36) Bouaamlat, H.; Hadi, N.; Belghiti, N.; Sadki, H.; Naciri Bennani, M.; Abdi, F.; Lamcharfi, T.-d.; Bouachrine, M.; Abarkan, M. Dielectric properties, AC conductivity, and electric modulus analysis of bulk ethylcarbazole-terphenyl. *Adv. Mater. Sci. Eng.* **2020**, *2020*, 1−8.
(37) Pickett, W.; Cohen, R.; Krakauer, H. Lattice instabilities, isotope effect, and high-T c superconductivity in La 2- x Ba x CuO 4. *Phys. Rev. Lett.* **1991**, *67*, 228−231.
(38) Ravikiran, U.; Sarah, P.; James, A.; Zacharias, E. Investigation of the role of Sm, Na in ferroelectric, piezoelectric and conduction behaviour of Strontium Bismuth Titanate ceramics. *Solid State Commun.* **2021**, *332*, 114309.
(39) Sharma, D. K.; Kumar, R.; Rai, R.; Sharma, S.; Kholkin, A. L. Impedance and modulus spectroscopy characterization of sodium-bismuth titanate-based lead-free ferroelectric materials. *J. Adv. Dielectr.* **2012**, *02*, 1250002.
(40) Yang, Y.; Kim, M.; Lee, S.; Choi, H.; Yang, Y. Impedance analysis and low-frequency dispersion behavior of Bi4Ti3O12 glass. *J. Korean Phys. Soc.* **2010**, *56*, 462−466.
(41) Chauhan, L.; Shukla, A.; Sreenivas, K. Dielectric and magnetic properties of Nickel ferrite ceramics using crystalline powders derived from DL alanine fuel in sol−gel auto-combustion. *Ceram. Int.* **2015**, *41*, 8341−8351.
(42) Jin, L.-W.; Su, Y. Effect of thermomechanical coupling on the scaling behavior of low-frequency hysteresis of PbZr0. 52Ti0. 48O3 ceramics. *Electron. Mater. Lett.* **2016**, *12*, 371−375.
(43) Tian, Y.; Wei, L.; Chao, X.; Liu, Z.; Yang, Z. Phase transition behavior and large piezoelectricity near the morphotropic phase boundary of lead-free (Ba 0.85 Ca 0.15)(Zr 0.1 Ti 0.9) O 3 ceramics. *J. Am. Ceram. Soc.* **2013**, *96*, 496−502.
(44) Venkata Ramana, M.; Roopas Kiran, S.; Ramamanohar Reddy, N.; Siva Kumar, K.; Murthy, V.; Murty, B. Investigation and characterization of Pb (Zr0. 52Ti0. 48) O3 nanocrystalline ferroelectric ceramics: By conventional and microwave sintering methods. *Mater. Chem. Phys.* **2011**, *126*, 295−300.
(45) Zhang, S.; Malič, B.; Li, J.-F.; Rödel, J. Lead-free ferroelectric materials: Prospective applications. *J. Mater. Res.* **2021**, *36*, 985−995.
(46) Zhang, T.; Du, J.; Lei, Y.; Cheng, Y.; Liu, W.; Yi, X.; Yin, J.; Yu, P. Effect of pores on dielectric breakdown strength of alumina ceramics via surface and volume effects. *J. Eur. Ceram. Soc.* **2020**, *40*, 3019−3026.
(47) Cai, Z.; Feng, P.; Zhu, C.; Wang, X. Dielectric breakdown behavior of ferroelectric ceramics: The role of pores. *J. Eur. Ceram. Soc.* **2021**, *41*, 2533−2538.
(48) Zhang, T.; Lei, Y.; Yin, J.; Du, J.; Yu, P. Effects of pores on dielectric breakdown of alumina ceramics under AC electric field. *Ceram. Int.* **2019**, *45*, 13951−13957.
(49) Yin, J.; Zhang, Y.; Lv, X.; Wu, J. Ultrahigh energy-storage potential under low electric field in bismuth sodium titanate-based perovskite ferroelectrics. *J. Mater. Chem. A* **2018**, *6*, 9823−9832.
(50) Sharma, S.; Sharma, H.; Kumar, S.; Thakur, S.; Kotnala, R.; Negi, N. Analysis of sintering temperature effects on structural, dielectric, ferroelectric, and piezoelectric properties of BaZr0. 2Ti0. 8O3 ceramics prepared by sol−gel method. *J. Mater. Sci.: Mater. Electron.* **2020**, *31*, 19168−19179.
(51) Xue, F.; Tang, L.; Guo, P.; Luo, Z.; Li, W. Multiferroic properties of BiFeO3−Pb (Zr0. 52Ti0. 48) O3 solid solution. *J. Mater. Sci.: Mater. Electron.* **2018**, *29*, 14285−14291.
(52) Liu, J.; Niu, M.; Wang, L.; Peng, C.; Xu, D. Effect of tuning A/B substitutions on multiferroic characteristics of BiFeO3-based ternary system ceramics. *J. Magn. Magn. Mater.* **2020**, *510*, 166928.
(53) Muneeswaran, M.; Akbari-Fakhrabadi, A.; Gracia-Pinilla, M. A.; Denardin, J. C.; Giridharan, N. V. Realization of structural transformation for the enhancement of magnetic and magneto capacitance effect in BiFeO3−CoFe2O4 ceramics for energy storage application. *Sci. Rep.* **2021**, *11*, 2265−2313.
(54) Mahesh, M.; Pal, P.; Prasad, V.; James, A. Improved Tunability and Energy Storage Density Properties of Low-Loss, Lead-Free (Ba0. 50Sr0. 50) TiO3 and Ba (Zr0. 15Ti0. 85) O3 Bilayer Thin Film Stacks. *J. Electron. Mater.* **2022**, *51*, 727−735.
(55) Qu, N.; Du, H.; Hao, X. A new strategy to realize high comprehensive energy storage properties in lead-free bulk ceramics. *J. Mater. Chem. C* **2019**, *7*, 7993−8002.
(56) Cheng, L.-Q.; Jiang, G.; Ma, Z.; Xu, Z.; Yu, M.; Lu, J.; Chen, K. Enhanced electrocaloric performance within wide temperature span in Al-doped BaZr0. 2Ti0. 8O3 ceramics. *J. Mater. Sci.: Mater. Electron.* **2022**, *33*, 24986−24994.
(57) Liu, B.; Wu, Y.; Huang, Y. H.; Song, K. X.; Wu, Y. J. Enhanced dielectric strength and energy storage density in BaTi0. 7Zr0. 3O3 ceramics via spark plasma sintering. *J. Mater. Sci.* **2019**, *54*, 4511−4517.
(58) Badapanda, T.; Chaterjee, S.; Mishra, A.; Ranjan, R.; Anwar, S. Electric field induced strain, switching and energy storage behaviour of lead free Barium Zirconium Titanate ceramic. *Phys. B* **2017**, *521*, 264−269.
(59) Samanta, S.; Sankaranarayanan, V.; Sethupathi, K. Effect of Nb and Fe co-doping on microstructure, dielectric response, ferroelec-

https://doi.org/10.1021/acsomega.2c06764
ACS Omega 2023, 8, 37752−37768

tricity and energy storage density of PLZT. *J. Mater. Sci.: Mater. Electron.* **2018**, *29*, 20383−20394.
(60) Gupta, A. K.; Sil, A. Effect of sintering temperature on spark plasma sintered PbZr0. 52Ti0. 48O3: Impedance and energy storage analysis. *Phys. B* **2021**, *601*, 412641.

https://doi.org/10.1021/acsomega.2c06764
ACS Omega 2023, 8, 37752−37768